FLUID UPTAKE OF THE GODDARD SHALE IN SOUTH CENTRAL OKLAHOMA, USA.

by

PAUL HUGGINS

Presented to the Faculty of the Graduate School of

The University of Texas at Arlington in Partial Fulfillment

of the Requirements

for the Degree of

MASTER OF SCIENCE IN EARTH AND ENVIRONMENTAL SCIENCES

THE UNIVERSITY OF TEXAS AT ARLINGTON

December 2015

Acknowledgements

I would like to personally thank and acknowledge my thesis advisor, Dr. Qinhong Hu, along with my thesis committee of Dr. Majie Fan and Dr. John Wickham. This thesis would not have been possible without their continual input and assistance along the way. I would also like to thank an oil and gas company which provided the samples and their representative who allowed me to use the data. They have been supportive throughout the entire process and were a pleasure to work with. I want to also thank the following members of Dr. Hu's research group who worked with and trained me on the procedures, they are Golem Kibria, Shawn Zhang, Troy Barber, Douglas Tebo, Francis Chukwuma, (Dean) Mengdi Sun and (Ray) Rui Yang. In addition, I want to thank Drilling Info for providing a complimentary subscription of DI Pro to the research group of Dr. Hu. Finally, I need to thank my family, friends, and fiancée; their constant words of encouragement and support were vital to this undertaking.

November 20, 2015

Abstract

FLUID UPTAKE OF THE GODDARD SHALE IN SOUTH CENTRAL OKLAHOMA, USA

Paul Huggins, MS

The University of Texas at Arlington, 2015

Supervising Professor: Qinhong Hu

The South Central Oklahoma Oil Province is the current play for the Goddard shale and is also the main field for the underlying Woodford Formation. As of September 2015, an estimated 40 wells have been drilled to evaluate and produce the Goddard shale in the southeastern portion of the Anadarko Basin. With companies reporting initial production rates ranging from 1,000 boe/d to nearly 2,000 boe/d and 30 day reports averaging around 800 boe/d, the amount of recovery from this tight shale reservoir has exceptional potential. Continental Resources Inc. estimates a gross recovery of 940,000 boe per lateral well. Understanding the reservoir quality and characteristics of the Chesterian-age Goddard shale is vital to understanding future production and exploration. There has been very little petro-physical work done on the Goddard shale due to the lack of overall production along with the declining oil prices at the time of discovery. Using hydrophilic (water and/or brine) and hydrophobic (n-decane) fluids, the purpose of this study is to examine wettability, fluid migration and pore connectivity of the Goddard shale. To achieve this, we collected core samples from two wells located at the heart of the play and performed wettability, fluid imbibition and vapor adsorption, and mercury injection capillary pressure tests. Results from these studies show that the Goddard shale has a strong affinity to oil (n-decane in this study) compared to DI water and API brine. With porosity values averaging 6% and permeability generally greater than

0.5 mD, the majority of pore-throat sizes for the Goddard shale are 0.005-0.01 μm, which is typical of organic pores rather than mineral pores which are generally larger. A petro-physical analysis of the shale based on the results of this thesis is beneficial to further understand the pore structure and fluid migration within the shale to facilitate increased production and accurate economic evaluations.

Table of Contents

List of Illustrations

List of Tables

List of Equations

Chapter 1

Introduction

The Goddard shale lies within the already producing South Central Oklahoma Oil Province (SCOOP) that boasts 5.1 billion barrels of liquid hydrocarbons and 135 trillion cubic feet of recoverable gas (Ball, 1991). According to Mitchell Henry and Timothy Hester, only 2.3 billion barrels of liquids and 65.5 trillion cubic feet of gas have been recovered, leaving more than double that still recoverable as of 1995 (Henry and Hester, 1995).

The currently producing major formations around the Goddard are the Caney, Sycamore and Woodford formations shown in Figure 1-1, each with their own petro-physical properties that allow for exploitation of hydrocarbons (Menchaca, 2014). This study evaluates the Goddard more effectively for production and economic value, and is vital for future exploration. Figures 1-1 and 1-2 below show a stratigraphic column of the SCOOP in the Anadarko Basin along with the known Goddard play area. The samples obtained for this study are from the two wells denoted as stars on Figure 1-2. These wells, along with the name of the company that supplied the samples, are to remain confidential. There are three distinct markers or beds within the Goddard shale that separate the Springer Sands above and the Caney shale below. Each marker varies in thickness and log characteristic. This study will explore the uppermost marker of the Goddard shale, to be referred to as M1 in this thesis.

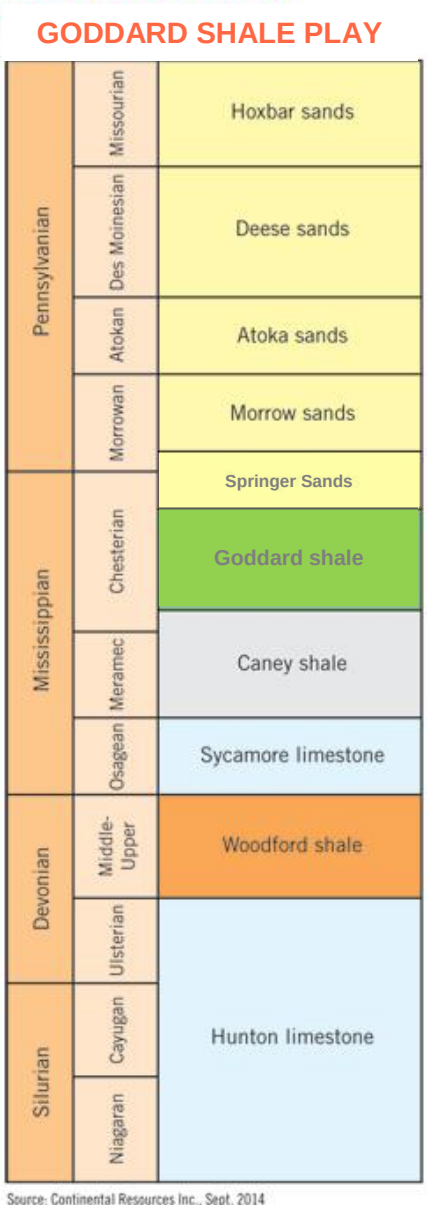

Figure 1-1 Stratigraphic Column of the South Central Oklahoma Oil Province (modified from Continental Resources, 2014).

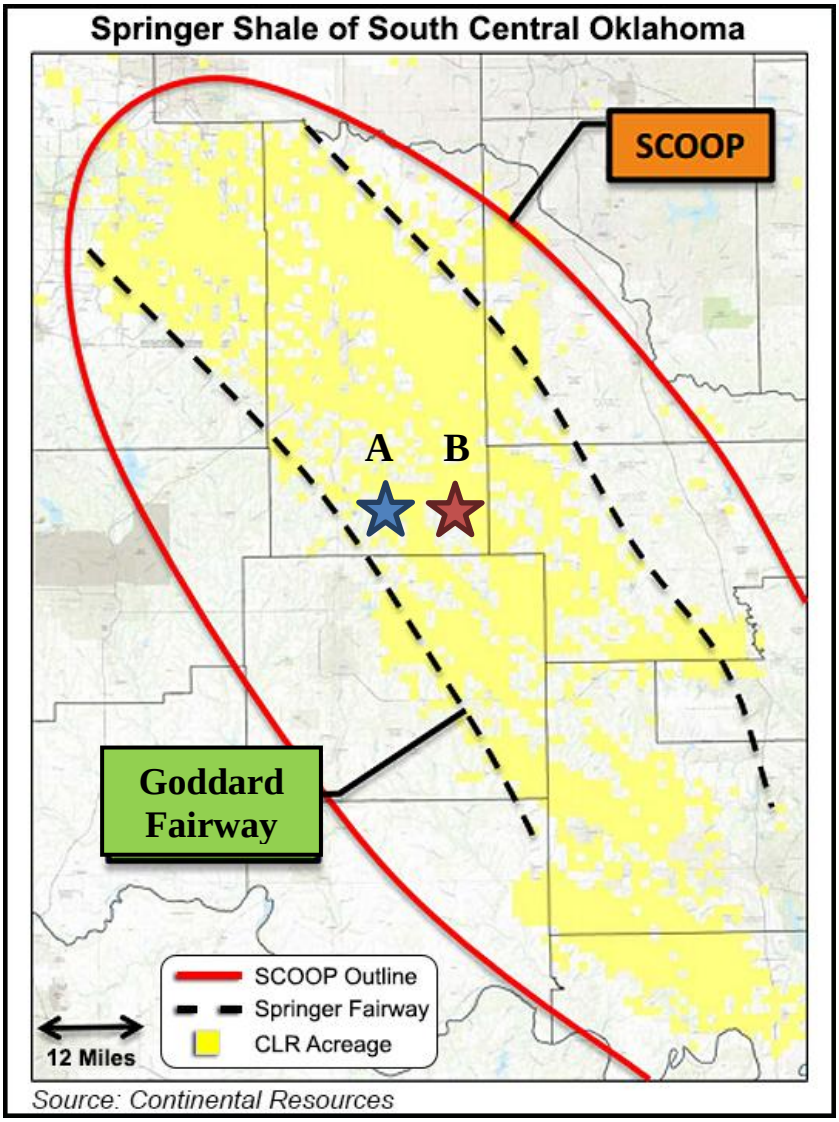

Figure 1-2 Goddard shale play outline within the SCOOP (South Central Oklahoma Oil Province) with the two wells (denoted A and B) with samples used in this thesis (modified from Continental Resources presentation, 2014).

Chapter 2

Geologic Setting and Depositional Environment

The Goddard shale for this study lies on the southeastern edge of the Anadarko Basin. The Anadarko Basin subsided during the Paleozoic and has faulting associated with the Wichita Orogeny that lasted from the Early Pennsylvanian until the end of the Permian (Ball, 1991; Johnson, 1988). It is bound to the east by the Nemaha Uplift, to the southeast by the Arbuckle Mountains and Ardmore Basin, and to the south by the Wichita Mountains and Amarillo Uplift (Ball, 1991). The basin is bounded to the west by the Cimarron and Las Animas Arches, to the north by the Central Kansas Uplift, and the Pratt Anticline to the northeast (Henry and Hester, 1995). Figures 2-1 and 2-2 are regional maps of the basin with the SCOOP area outlined, and Figure 2-3 is a cross section showing the structure of the Southeastern Anadarko Basin. The basin covers about 58,000 square miles and is the deepest basin in the cratonic U.S. (Ball, 1991). The stratigraphy in the area ranges from the Cambrian to the Permian and reaches more than 11.5 km in the deepest parts of the basin (Brewer, 1983). There are also Mesozoic and Cenozoic sedimentary rocks toward the northwest overlying the Paleozoic strata (Ball, 1991). Carbonates make up the older parts of the basin that start at the Cambrian and continue intermittently through the Mississippian, while sandstones and shales make up the younger parts of the basin (Ball, 1991). The volume of sandstones increases towards the southern part of the basin due to the synsedimentary faulting producing the Wichita Mountain Belt as shown in Figure 2-3.

The Springer Group is of Mississippian and Pennsylvanian age and consists of sand bodies with interbedded shales with a maximum thickness of about 6,000 feet (Tomlinson and McBee, 2014; Ball, 1991; Peace, 1965). The Cunningham, Britt, Spiers, Boatwright, and Goddard make up the formations of the Springer Group (Boyd, 2008;

Chrisman, 2009; Rice, 1993). These sands are believed to have originated from the Wichita Mountain uplift from the south, creating deep water submarine fans (Ball, 1991; Bennison, 1956; Wilson, 1996). Possible reservoirs within the Springer Sands can be derived from upper and middle fan channels, sheet sands, feeder-channels, and distal-fan sheet sands (Hugman and Vidas, 1987). The Goddard shale lies at the base of the Springer Group, and is associated with the Noble Ranch Group, nearing the end of the Chesterian Age, as supported by lithology and fauna fossil presence (Elias, 1957; Smith, 1995; Straka, 1972; Westheimer, 1954). It is believed that the Goddard was deposited during a sea level regression and correlates to a deep water submarine fan (Ball, 1991; Blakey, 2014).

Figure 2-1 Anadarko Basin Regional Map (Drilling Info, 2015).

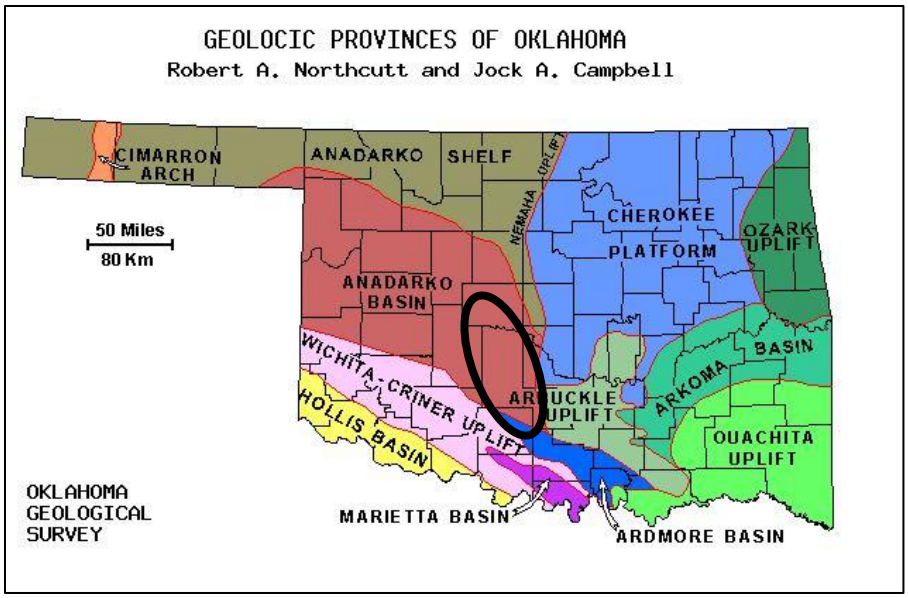

Figure 2-2 Regional Map of the Anadarko Basin (Northcutt and Campbell, 1995).

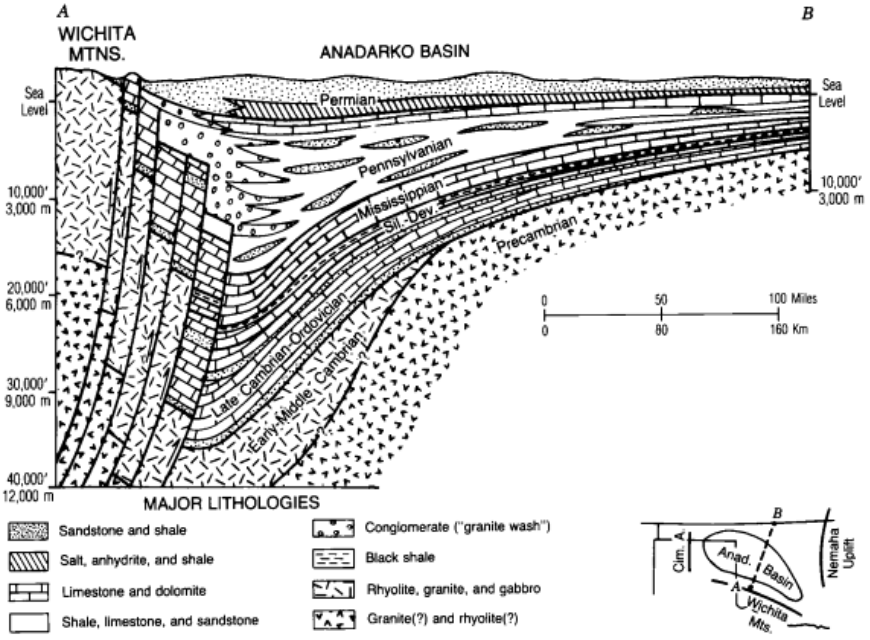

Figure 2-3 Regional Cross Section of the Anadarko Basin (Lee and Deming, 2002).

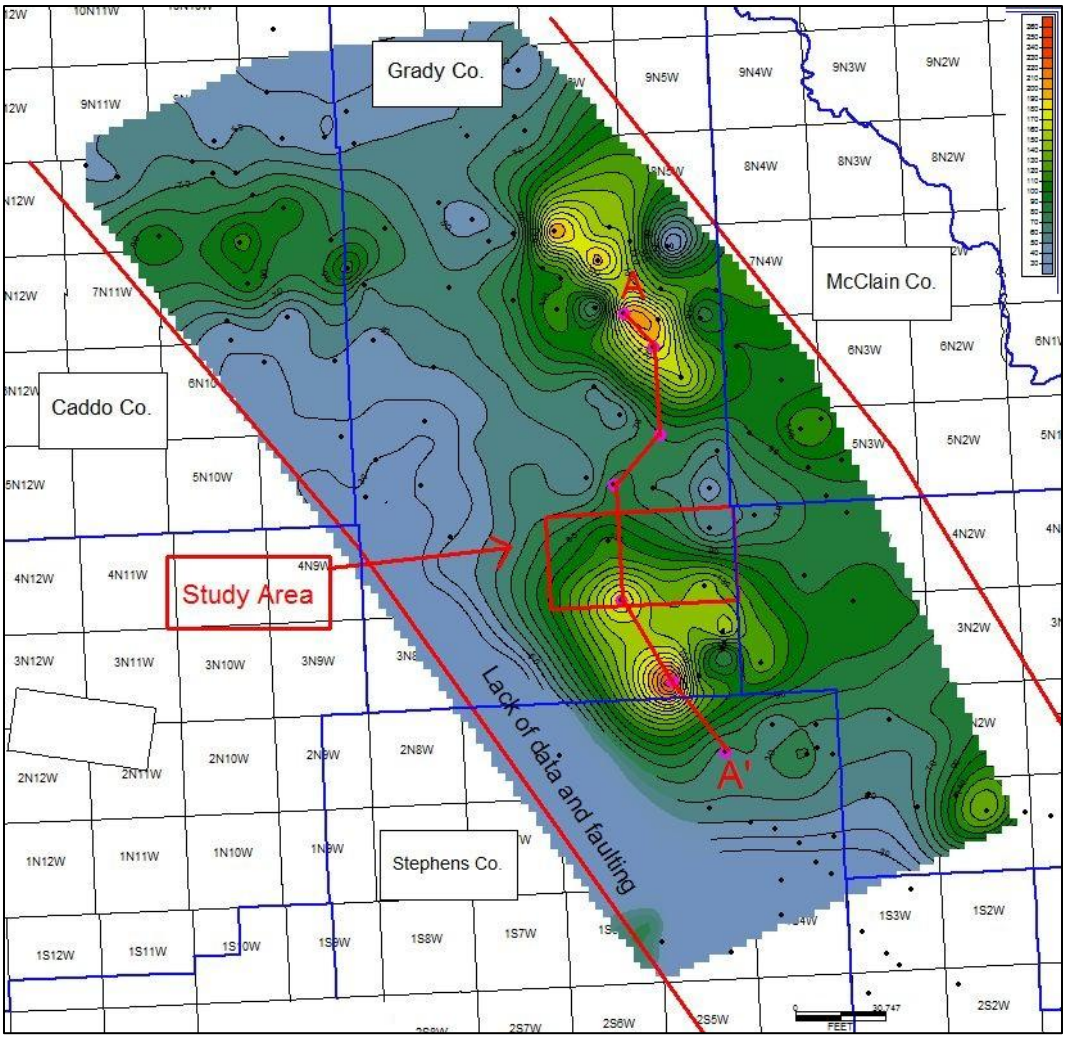

Figure 2-4 Goddard shale Isopach Map. CI = 10' with cross section through A-A' shown. Thickness ranges from 20 (blue) to 250 (red). (*Disclaimer*: this map was created in conjunction with Expro Minerals and intended acquisition purposes only, releasing them of any liability that may occur from misinterpretation or misuse).

2-1 Well Log Interpretation

There are three Goddard shale “markers” above the Caney Formation and below the Springer Sands. Each marker has its own unique characteristics and log signature. While the uppermost marker is the target of this study, it is necessary to define its’ extent. To pick the Goddard shale on logs, the gamma ray and resistivity curves are the key, with the density-neutron curves providing additional data when needed. A cross section was constructed (Figure 2-6) with the location shown on Figure 2-5. The cross section does not cover the entire Anadarko basin, but covers the area of the SCOOP being targeted by producers in the area. There is a depressed gamma ray signature in the Goddard shale that may be caused by low uranium and thorium counts causing the shale to appear less radioactive and “hot”. The majority of Goddard production follows the cross section line A-A’ shown in Figure 2-4. The log characteristic of the uppermost Goddard shale changes depending on location in the SCOOP. Typical log characteristics show a gamma ray signature hovering around 90-130 API with spikes up 150-200 API. A fluctuating resistivity value of 25-50 ohms is associated with the Goddard as well. There is generally a spike in gamma ray and sharp decrease in resistivity at the base. Moving northwest from A-A’, the formation becomes cleaner, indicating more sand presence at deposition. The cross section (Figure 2-6) shows from stratigraphic top to stratigraphic bottom: M1 (target of study in this thesis), Caney, and Woodford formations.

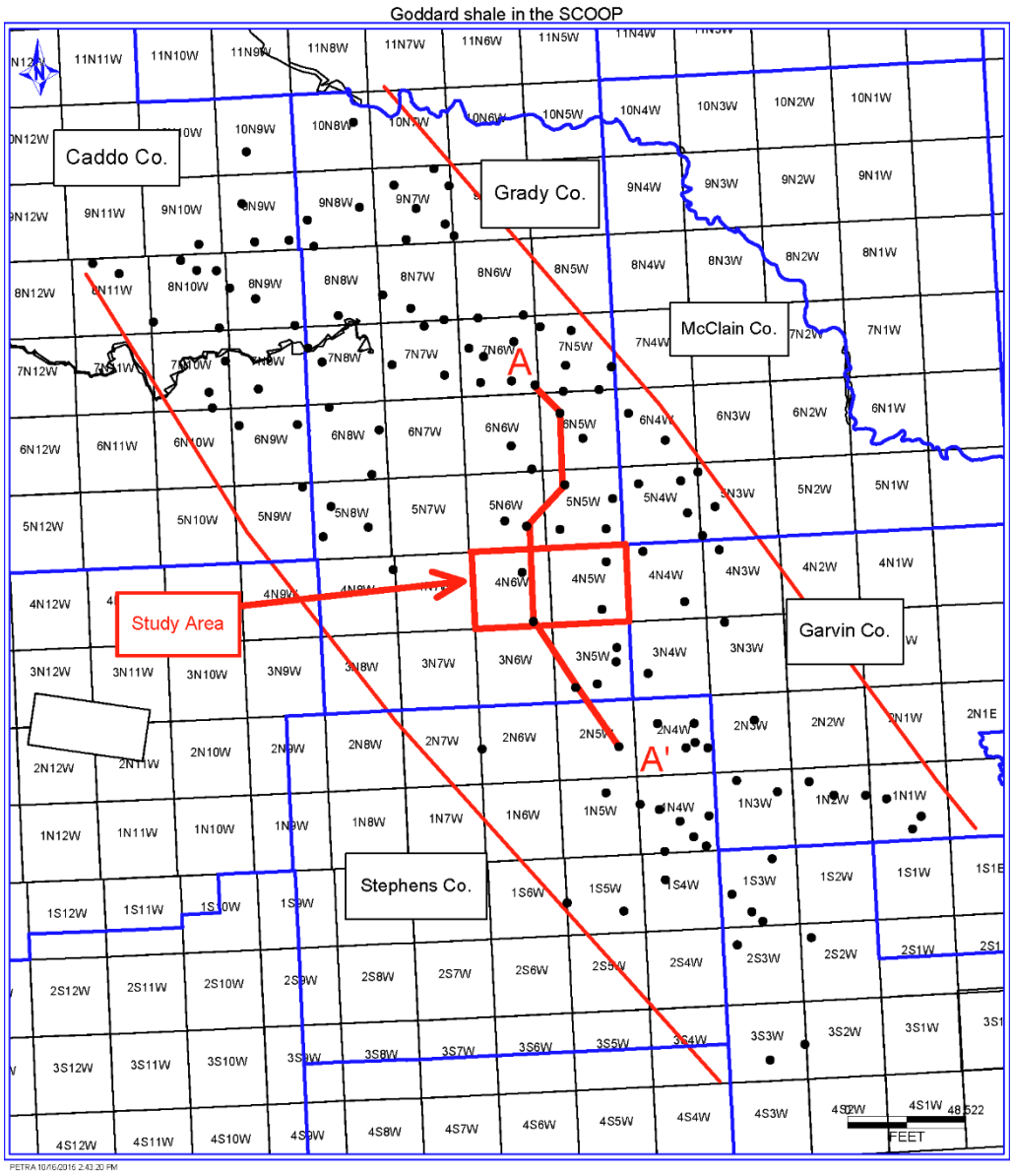

Figure 2-5 Cross Section through A-A' Mapping the Goddard (M1), Caney, and Woodford Formations.

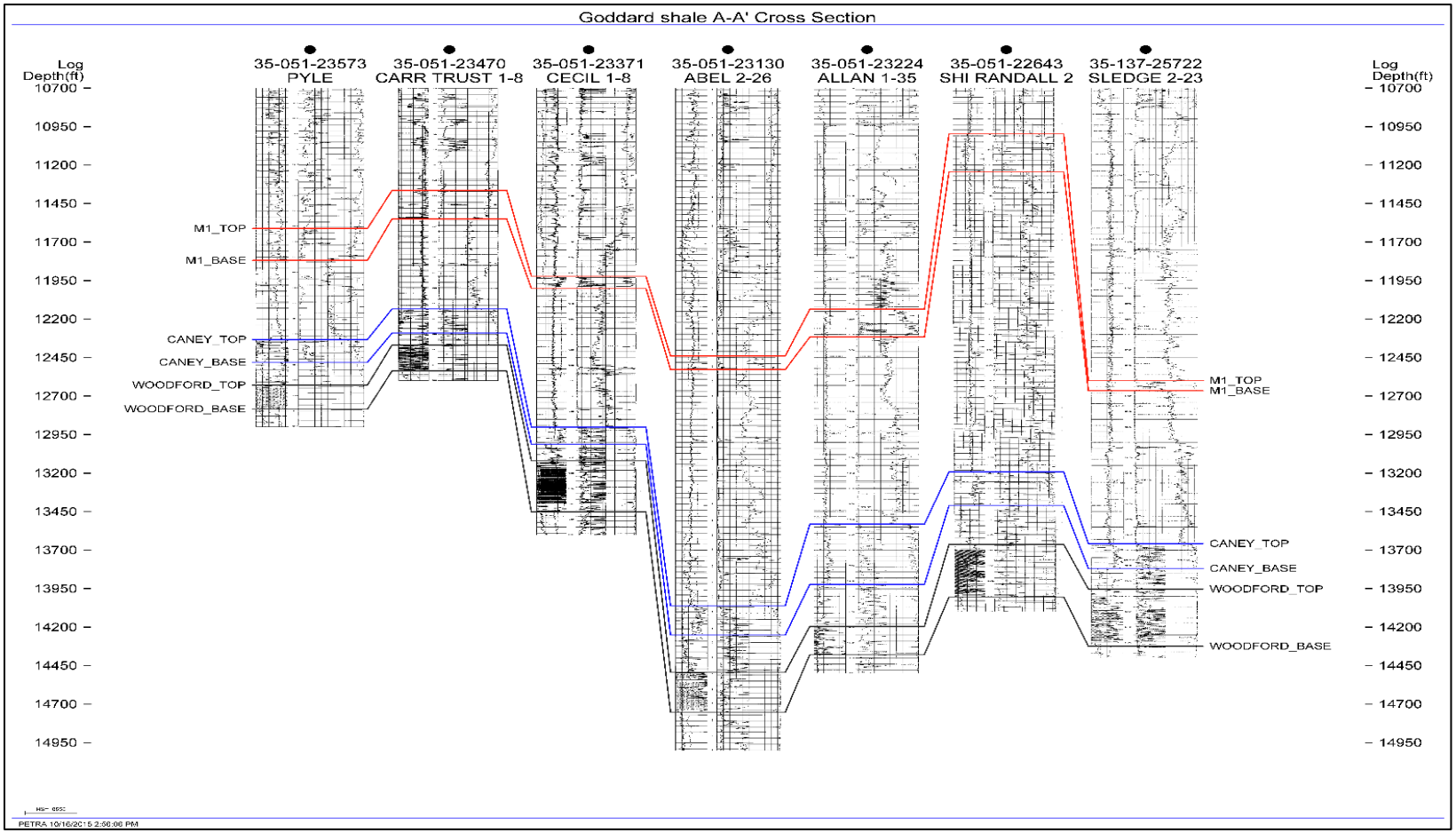

Figure 2-6 Well Log Interpretation of the M1, Caney, and Woodford Formations.

Figure 2-7 is a type log from Triad Energy's Cecil 1-8 well drilled in 2006 located in Township 5 North, Range 5 West, about 6 miles north of the study area (Oklahoma Corporate Commission, 2015). The log signature is typical of the Godard in the area and shows the variable gamma characteristic with the strong resistivity presence.

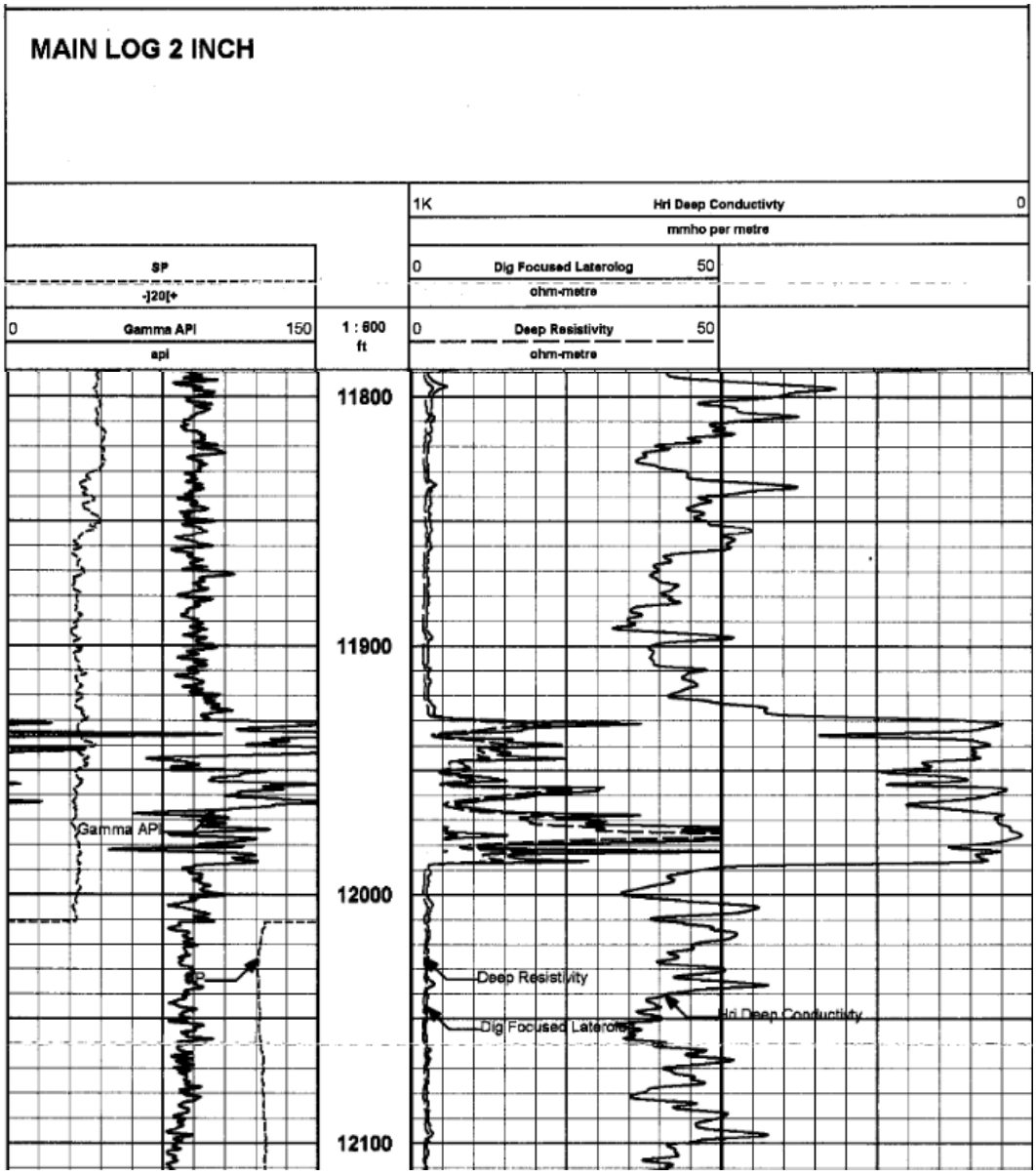

Figure 2-7 Cecil 1-8 Type Log over the Goddard interval.

Chapter 3

Methods

3-1 Acquisition of Shale Samples

As the target of this study, the Goddard shale consists of organic rich, gray, soft, siliceous to argillaceous fissile shale (Laudon, 1958). Core samples were obtained from Grady County, Oklahoma, Township 4 North and Range 6 West, and from Township 4 North and Range 5 West (Table 3-1).

Table 3-1 Approximate Location of Shale Samples

Well Name	County	Location (Township and Range)	Depth of Core 1 (Measured Depth Feet)	Depth of Core 2 (MD Feet)	Depth of Core 3 (MD Feet)
A	Grady	4N, 6W	12809.0'	12847.0'	12871.0'
B	Grady	4N, 5W	12945.8'	13010.1'	13046.8'

The samples from well A consisted of 3 sidewall cores from depths of 12,809', 12,847', and 12,871', shipped in sample tubes with cushioned packaging. The samples from well B came from depths of 12,945', 13,010', and 13,046' and were hand cut from a whole core and significantly larger-sized than those from well A. The sample names from the wells are listed in Table 3-2. The OK Springer prefix assigned to the samples is synonymous with the Goddard shale. Sample OK Springer U arrived as black circular conglomerate of shale and drilling mud that crumbled immediately upon handling and was cleaned with DI water prior to testing, although only a few fragments were usable.

Table 3-2 Shale Samples with Identification and Weight upon Arrival

Sample ID	Arrival Weight (grams)
OK Springer U	30.0
OK Springer M	56.5
OK Springer L	60.4
OK Springer 2U	315.0
OK Springer 2M	138.4
OK Springer 2L	146.3

Photos were taken with the digital and microscope camera before the cutting procedure began. The lighting conditions were not uniform for all the photos, therefore the image colors are not comparable. The (A) photos were taken after removal from shipping packaging. The (B) photos were taken under a microscope zoomed in on the entire sample.

(A)

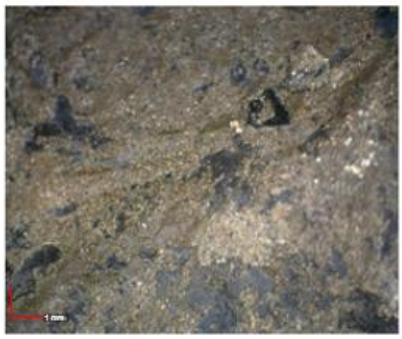

(B)

(A)

(A)

(B)

(B)

(A)

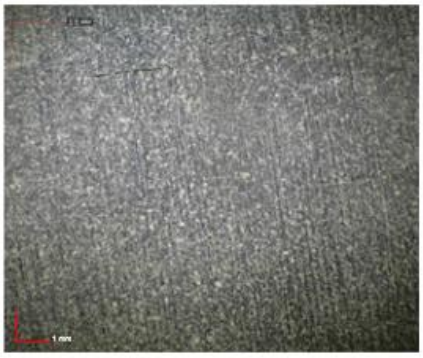

(B)

(C)

(A)

(B)

(D)

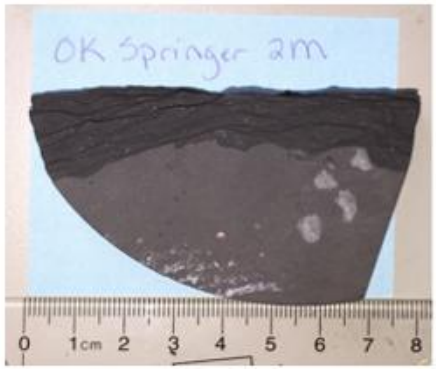

(A) (B)

(E)

(A) (B)

(F)

Figure 3-1 Sample Photos upon Arrival. (A) Zoomed out (B) Zoomed in (scale bars are all shown on the pictures) (A) OK Springer U; (B) OK Springer M; (C) OK Springer L; (D) OK Springer 2U; (E) OK Springer 2M; (F) OK Springer 2L.

Following the photographing, the samples were marked with a red pencil to denote lamination direction. The samples were then dry cut using a circular saw into 6, 1cm sided cubes from each depth range; 6 cubes from the upper, 6 from the middle, and 6 from the lower section in each well. The red pencil mark was intended to be visible after cutting, and was used to identify and mark the top and bottom of the sample from the lamination direction (Figure 3-2). The bottom of the sample, labeled "B," was to be the main side for testing of fluid imbibition and DI water vapor adsorption. The top of the sample was labeled "T" and represented the face transverse to lamination and opposite of the base. The B and T faces are representative of testing faces and have no relation to stratigraphic top or bottom. Each cube was epoxied on every face except for the T and B faces to allow for 1 dimensional flow through the sample during testing. The cut samples were assigned a number 1 through 6 to denote which tests to be done on each sample. Six cubic samples from the upper, middle, and lower sections from each well were used for this thesis (i.e. 18 cubes from each well), sample numbers 5 and 6 are to be used for later research. Figures 3-2 shows an example of this sample processing step. The samples were then measured for their individual dimensions and weighed to note changes during testing.

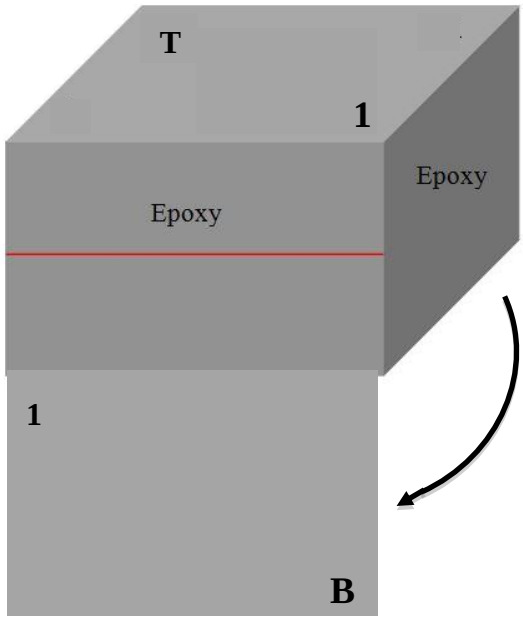

Figure 3-2 Sample Labeling and Epoxy.

Once the samples were cut and labeled, they were epoxied on the 4 exterior sides (excluding B and T faces) to constrain flow through the sample to 1 dimension during testing. MICP samples were not epoxied. Epoxying 4 of the 6 sides limits imbibition and evaporation through the sides of the sample. Following the epoxying of the samples and before testing, they were left to dry for 24 hours for epoxy to cure before being placed in glass vials and placed in a 60^{o} C dry oven to complete the drying process. Once completely dry, the vials were removed from the oven and placed in a desiccator with low humidity to be stored until testing. Table 3-4 denotes which sample numbers were assigned to each test.

Table 3-3 Sample Numbering and Associated Lab Tests.

Sample Number	Associated Test
1	DI Water – Fluid Imbibition and Vapor Adsorption
2	API Brine Imbibition with tracers
3	N-Decane Imbibition with tracers
4	MICP

3-2 Wettability

The wettability test observes the surface wetting characteristics of the sample and determines whether the shale is wetting or non-wetting to de-ionized water, n-decane or API brine. This test was conducted with flat fragments recovered from the cutting process lacking in visible cutting marks, not one of the six cubes. The DI water samples were dried off and reused, while the n-decane and API brine samples were discarded. One drop of fluid (15 μL) from a pipette was used to wet the surface of each sample to observe the spreading of the liquid. A number was assigned for the spreading behavior over 30 seconds; t, number 1 designating no spreading at all, while the number 10 representing perfect spreading of the fluid on the sample. Each sample was photographed and recorded during testing using a microscope camera.

3-3 Mercury Injection Capillary Pressure (MICP)

The MICP approach involves the use of non-wetting mercury applied at a pressure of up to 60,000 psia (413 Mpa) to overcome the capillary pressure and invade the pores of the shale samples. The University of Texas at Arlington possesses the MICP instrument (Micromeritrics Autopore IV 9510, Norcross GA). Mercury Porosimetry is done by applying increasing levels of pressure to a sample surrounded by mercury (Zhou,

2010). As the pressure increases, the smaller the pore throats are invaded, thus creating a distribution curve of pore sizes (Hu and Ewing, 2014; Kaufmann, 2010). The range of pore sizes able to be detected is 3 nm to 30 µm in diameter for tight shale samples. This method characterizes the samples total pore surface area, total volume, tortuosity, and median or mean pore diameters (Hu and Ewing, 2014; Hu et al., 2015; Micrometrics, 2011; Swanson, 1981).

The laws governing capillary pressure determine the capability of Mercury Porosimetry (Hu et al., 2015a). Mercury is unique in that it acts as a non-wetting fluid in porous media, requiring external pressure to invade pore throats. The Washburn equation is used to determine the pressure to pore throat relationship assuming that the pores are cylindrical (Washburn, 1921).

$$\Delta \boldsymbol{P} = -\left(\frac{\boldsymbol{2ycos\Theta}}{\boldsymbol{R}}\right) \quad \text{.....(3.1)}$$

Where,

∆P – Difference in pressure across the curved mercury interface (psia);

Y – Surface tension for mercury (485 dynes/cm);

Θ – Contact angle between the porous medium and mercury;

R – Corresponding radius of the pore throat using Y and Θ

The equation above, using the variables, can be simplified to:

$$\Delta \boldsymbol{P} = -\left(\frac{\boldsymbol{90.43}}{\boldsymbol{R}}\right) \quad \text{.....(3.2)}$$

Where,

R – Pore throat radius in µm (Gao and Hu, 2012; Hu and Ewing, 2014).

The MICP machine collects data during the test regarding applied pressure and induced intrusion at the specific pressure (Gao and Hu, 2012; Hu and Ewing, 2014). This

equation assumes that pores are cylindrical, this is rarely true in the real world, but it provides a representation of the pore distribution in the sample that is useful in applications.

The MICP machine not only measures the inverse relationship between pore throats and pressure, it is also useful in determining permeability. To determine permeability, the Katz and Thompson (1986; 1987) equation calculates permeability using the applied pressure and intrusion volume measurements from the MICP data.

$$\mathbf{k} = \left(\frac{\mathbf{1}}{\mathbf{89}}\right)(\mathbf{L_{max}})^{\mathbf{2}}\left(\frac{\mathbf{L_{max}}}{\mathbf{L_c}}\right)\mathbf{\Phi S}(\mathbf{L_{max}}) \quad \text{.....(3.3)}$$

Where,

K – Sample permeability to air (µm);

$(\mathrm{L_{max}})$ – Pore-throat diameter when hydraulic conductance is at a maximum (µm), when mercury starts to percolate the whole sample;

$\mathrm{L_c}$ – Length of pore throat diameter (µm) corresponding to threshold pressure (taken from inflection point on intrusion curve) (psia);

Φ – Porosity of the sample;

$S(L_{\max})$ – Mercury saturation at percolation $(L_{\max})$ (Gao and Hu, 2012).

Calculating tortuosity comes from the MICP data using the equation of Hager and Webb (Hager, 1989). Tortuosity is related to effective diffusion coefficient and travel distance of molecules (Hu et al, 2015a).

$$\boldsymbol{\tau} = \sqrt{\frac{\boldsymbol{p}}{\boldsymbol{24k(1+pV_{tot})}}\int_{\boldsymbol{n=r_c,min}}^{\boldsymbol{n=r_c,max}} \boldsymbol{n^2 f_v(n)dn}} \quad \text{.....(3.4)}$$

Where,

τ - Tortuosity

P – Density of mercury (g/cm^3)

V_{tot} – Total pore volume (mL/g)

$\int_{n=r_c,min}^{n=r_c,max} n^2 f_v(n) dn$ – Pore throat volume distribution by pore-throat size calculated by MICP.

Procedure for MICP Tests

The 1 cm^3samples from each well were originally oven dried at 60° C for at least 3 days to remove any residual moisture in connected pore spaces. They were then placed in a desiccator at 23° C and allowed to cool to room temperature while keeping the humidity below 10% to avoid any moisture intruding the sample during the cooling process before the MICP analysis (Hager, 1998). To begin the testing, the sample is placed into a penetrometer. The penetrometer is an apparatus consisting of a sample chamber connected to a metal precision-bore and glass capillary system. Once the sample is sealed inside, the entire penetrometer apparatus is placed in a low pressure chamber that is evacuated to 50 µm Hg (0.05 torr, 0.000972 psi, 6.7 pa). The evacuation process removes any access air or moisture that entered the machine during the setup process, as well as inside the sample. After the evacuation is complete, the sample undergoes both low-pressure and high-pressure analyses. The low-pressure analysis involves filling the sample chamber with mercury to a maximum of 30 psia and equilibrium time. The equilibrium time is the minimum time for the Mercury to stabilize within the sample before the next pressure is applied (Chukwuma, 2015). The equilibrium time during the low-pressure testing is set to 10 seconds for shales. As the mercury invades the sample, it overcomes the capillary pressure and invades the larger pore throats that average a diameter of about 30 µm (dependent upon the choice of the penetrometer). In high-pressure testing, the pressure is increased in steps from 30 psia up to 60,000 psia with an equilibrium time or 45 seconds for each step. The high-

pressure analysis allows the mercury to invade pore throats as small as 3 nm. The MICP instrument records the volume of mercury invading the sample at each pressure applied. Using the physical properties of mercury (interfacial tension), the contact angle between mercury and the sample, pore throat radii, porosity, permeability and tortuosity can be calculated (Gao and Hu, 2012; Hu and Ewing., 2014). There is one important note regarding the MICP analysis. When determining pore size distribution, the ink-bottle phenomenon is observed (Chukwuma, 2015). This phenomenon is the connection between smaller pores on the surface that connect to larger pores within the sample. Issues with pore accessibility arise and can cause the machine to underestimate the amount of large pores and overestimate the amount of smaller ones (Hu and Ewing, 2014).

3-4 Fluid Imbibition and Vapor Adsorption

Fluid imbibition can either be forced via an external applied pressure, or spontaneous if the sample pores are wet with the same type of imbibed fluid (Lopez and Soria, 2007; Chaudhuri, 2010). The process of spontaneous imbibition is controlled by capillary forces within the porous media as the fluid is imbibed (Ma, 1999; Xie, 2001). The rate at which the fluid is imbibed is controlled by the porosity of the media, the wetting fluid, and the interaction between the media and fluid itself (Buckley, 1942). Three fluids (DI water, API brine, and n-decane) were used to study spontaneous imbibition in the Goddard shale. This study demonstrates the pore connectivity of the formation, along with the interaction between different fluids in the sample. While this test is relatively quick (24 hour average), the three fluids provide a model for the overall reservoir quality of the formation by using percolation theory (Mattox, 1962). Pore connectivity via percolation theory is estimated by graphing the slope of log imbibed liquid versus log time

(Chukwuma, 2015). The range of calculated slopes indicates the general connectivity of the pores. The beginning of the tests generally have a higher slope (+0.5) due to the edge accessible porosity in direct contact with the sample that are filled first. As the test continues, the slopes become lower in value due to the fluid moving its way through the sample only via connected pore spaces. If the slope becomes a negative number or zero, the fluid has either stopped moving through the pores, or the fluid front has reached the sample top.

Procedure for Fluid Imbibition and Vapor Adsorption Tests

This section details the procedure used in the imbibition and vapor tests. The $1\ cm^3$ samples were initially dried in the 60^{o}C oven for a period of at least 48 hours. Once testing is ready to begin, the desired sample was removed from the oven and placed inside a desiccator for more than 10 minutes to keep the humidity constant and avoid unnecessary moisture adsorption before testing when cooling the sample. While the sample was cooling, a petri dish (14.64 cm diameter and 1.90 cm height) was filled half full with the desired testing fluid (DI water, API brine, or n-decane), and weighed and recorded. Once the petri dish and fluid weight is recorded, the dish is placed inside a closed chamber beneath the electric scale as seen in Figure 3-3. For DI water or brine tests, there are two cups filled with water inside the chamber which keep the humidity constant throughout the test. The chamber itself rests on an adjustable base that moves in the vertical direction by a twistable lever at the base. The electric scale used is the Shimadzu AUW 220D and consists of a weighing plate inside the glass box and a hook beneath the scale that weighs the sample hanging beneath. The electric scale is connected to a computer that uses an Excel file to record the weight of the sample at specific time intervals over the time of the test.

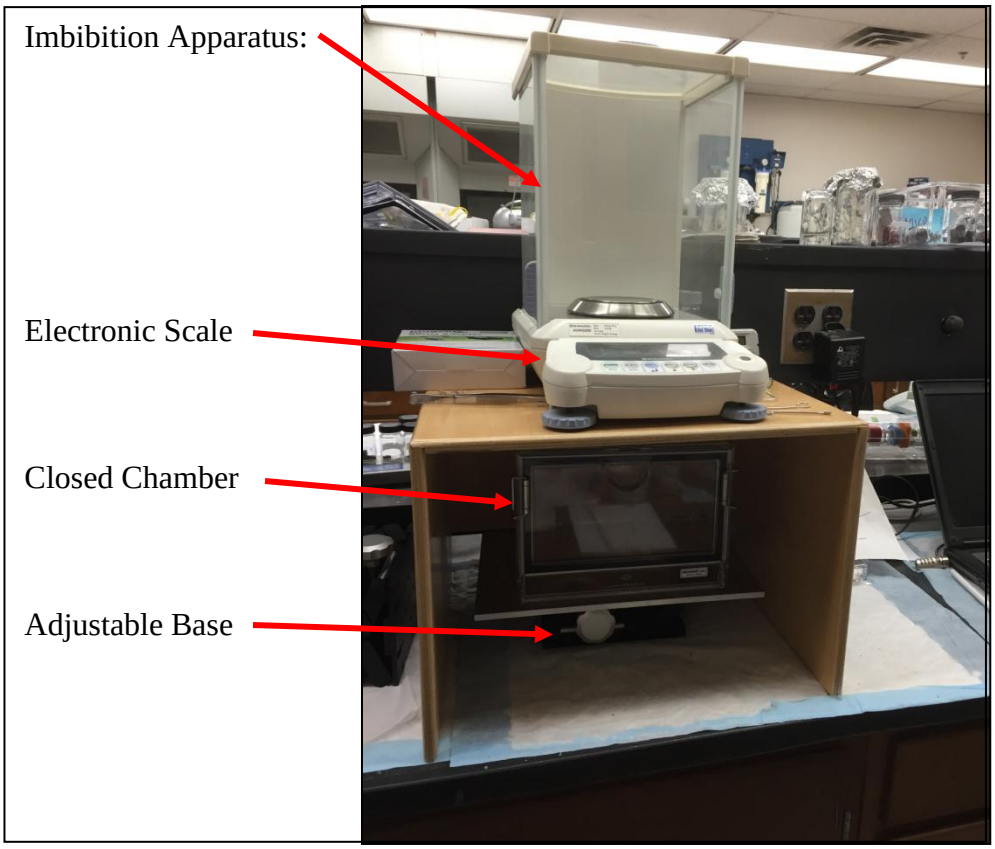

Figure 3-3 Imbibition and Vapor Adsorption Setup.

After the sample has been inside the dry keeper for more than 10 minutes, the sample is weighed using the scale and then placed inside a sample holder composed of a plastic cap and screws that secures the sample to avoid the sample being submerged in the fluid. Aluminum foil is placed inside the holder between the contact of the holder and the exposed sample top face. The sample holder is weighed, and hung inside the chamber. The hanging sample was completely still before testing began to avoid inaccurate data at the beginning of the test due to the motion of the apparatus. Once the sample is no longer moving and the scale and computer are set up, the test can begin. As shown in Figure 3-4, the sample remains in the same position while the adjustable

base is raised towards the sample. For imbibition, the base is raised until the lower 1-2 mm of the sample is submerged in the fluid. Vapor adsorption is set up the same way, but the sample is not submerged and hangs roughly 2-4 cm above the fluid. The imbibition experiment was repeated over time periods of 12 hours, 24 hours, and 48 hours, while the vapor adsorption test lasts for 7 days.

The scale was instructed to send data to the computer and log the sample weight change over the testing period. Once the test begins, weights are sent to the computer every 1 second for 2 minutes, then every 30 seconds for about 1 hour, followed by every 2 minutes for about 6 hours. The final interval for imbibition is 5 minutes for the remainder of the test, generally 18 hours. For vapor adsorption, at the 24 hour mark, the interval is set to record every 10 minutes and 1 second for the remaining 6 days of the test. Spot checks are taken during the tests to verify the data once the test is completed. The spot checks consist of recording the time of the check, weight at that time, and the clicker number associated with when the data was recorded and in what order compared to previous data.

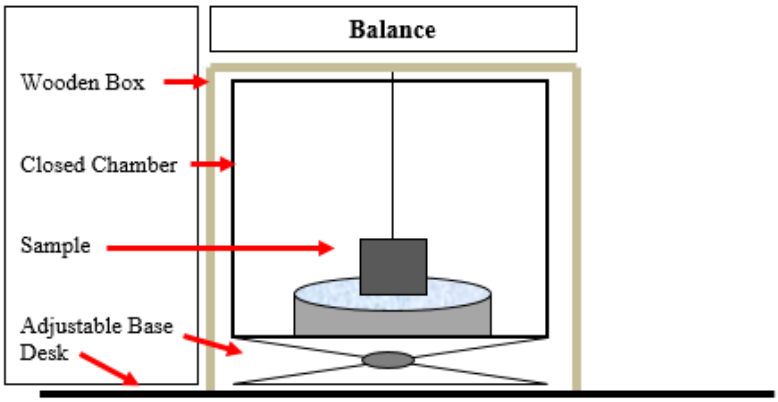

Figure 3-4 Imbibition Test Setup.

The testing fluids (DI water, API brine, or n-decane) each have distinct characteristics that make them valuable testing fluids. DI water was used to determine

the general pore connectivity of the sample and observe how long it took the fluid to pass through the entire sample, if at all. Once this time frame was determined, the other fluids testing periods were adjusted accordingly, knowing that n-decane would move through the samples at a quicker rate, from the wettability tests. N-decane was used on certain samples in conjunction with tracers to examine the movement of this hydrophobic fluid in organic matter pore systems.

Once the desired testing time is completed, the final weight of the sample is recorded and the scale is turned to the stand-by mode which stops the recording. A Kimwipe is slightly wetted with the testing fluid and weighed. The sample and sample holder are removed from the chamber and the Kimwipe is dabbed on the face of the sample that was submerged in the fluid to catch any residual fluid that may be adhered to the face of the sample. The Kimwipe is then weighed again to record any weight change from contact with the sample. The sample and holder are weighed, along with the sample itself. The petri dish with fluid is weighed next to observe the fluid loss from the dish. Once the final measurements have been taken and recorded, the data processing and analysis of the test results begins. To evaluate imbibition behavior, the Philips Infiltration Equation and the Handy Equation are used. These equations are based on the assumption that there is good pore connectivity (about 0.5 slope in log imbibed mass vs log imbibition time), therefore, they are more commonly used for n-decane imbibition opposed to DI water and API brine.

The Philip's Infiltration Equation utilizes infiltration data and sorptivity to calculate cumulative infiltration (Philip, 1957). Sorptivity is the function of initial and boundary water content.

Philip's Infiltration Equation

$$\mathrm{i} = \frac{1}{2}\mathrm{St}^{-0.5} \quad \text{.....(3.5)}$$

$$I = St^{0.5} \quad \text{.....(3.6)}$$

Where,

i – Infiltration rate

S – Sorptivity

t – Infiltration time

I – Cumulative Imbibition

The Handy Equation assumes that the weight or volume of the imbibed water is proportional to the square root of the imbibition time (Handy, 1960). This equation also assumes zero gravity and that imbibition occurs in a piston-like manner.

$$N_{wt}^2 = \frac{A^2\left(P_c k_w \phi S_{wf}\right)}{\mu_w} t \text{.....(3.7)}$$

Where,

N_{wt}^2 - Volume of water imbibed into the sample

A - Cross-section area of sample

P_c - Capillary Pressure at S_{wf}

k_w- Effective permeability of water at S_{wf}

Φ - Porosity

S_{wf} - Water saturation behind the imbibition front

t - Imbibition time

μ_w - Viscosity of water

Chapter 4

Results and Conclusions

4-1 Wettability

The results from the wettability experiments using DI water, API brine, and n-decane are discussed below. On a scale of 1 to 10, 1 being no spreading at all and 10 being perfect spreading across the sample, the samples from both wells had values of 9 and 10 for n-decane (Table 4.1) so were oil wetting, indicating that the shale could act as reservoir rock due to the high amounts of n-decane imbibed into the face. The lower DI water and API brine values (Table 4.1) reinforce this because to the shale prefers to absorb n-decane. Photos shown in Table 4-2 show the end result from each test. Other shales previously examined in the lab have lower DI water values commonly around 1-2 demonstrating almost no spreading behavior. The Goddard is noticeably higher, indicating a lower surface tension and the possibility that the shale could take in more water than desired during hydraulic fracturing.

Table 4-1 Wettability Test Results

Sample Name	DI Water Wettability Scale	API Brine Wettability Scale	N-Decane Wettability Scale
OK Springer U	7	3	10
OK Springer M	6	2	10
OK Springer L	7	2	10
OK Springer 2U	8	3	10
OK Springer 2M	5	5	9
OK Springer 2L	8	5	9

Table 4-2 Wettability Test Result Photos

Sample ID	DI Water Wettability	API Brine Wettability	N-Decane Wettability
OK Springer U	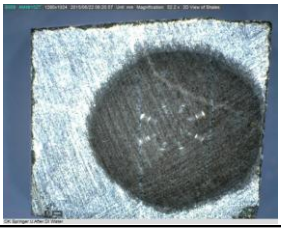		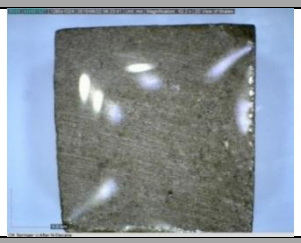
OK Springer M	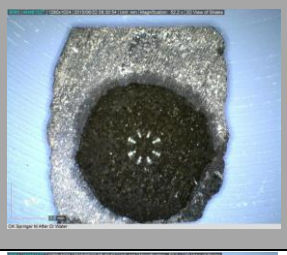	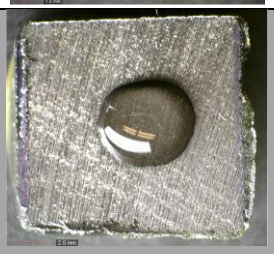	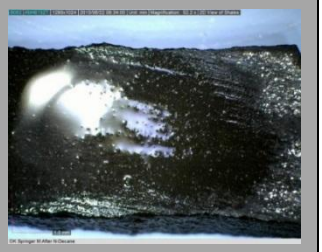
OK Springer L	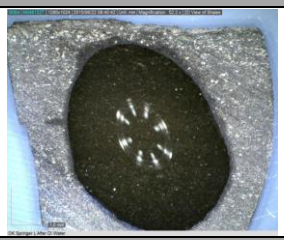		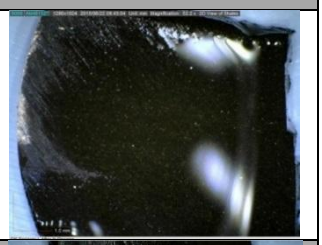
OK Springer 2U			
OK Springer 2M			
OK Springer 2L			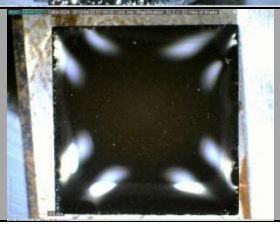

4-2 Mercury Injection Capillary Pressure (MICP) Results

MICP provided the petro-physical data for the Goddard shale including porosity, permeability, bulk density, and pore sizes. Table 4-3 shows the results of the MICP analysis. The sample OK Springer U was encased in drilling mud upon arrival and MICP was run on a cleaned fragments. Overall the Goddard shale has a porosity range of 2.47% to 6.90% and permeability in mD of 0.259 to 0.896. The higher porosities are found in the upper and middle Goddard while the lower Goddard has a lower porosity in both wells. Well A does not show much change in porosity over the section, while Well B shows a drastic difference between the middle and lower sections. Permeability does not show a general trend, but the lower section in Well B has the smallest porosity with the largest permeability. Bulk density of the Goddard ranged from 2.278 to 2.666 (g/cm^3), with the larger densities associated with the shallower samples. By comparing depth of sample and porosity, there are similarities seen in both wells. The middle depth sample in both wells shows the highest porosity for that section while the deepest sample shows the lowest porosity as seen in Figure 4-1. This trend could merely be a coincidence and needs further work to support a conclusion. Figure 4-2 shows porosity vs density for the samples. With the exception of OK Springer 2L, the higher porosities correlate to a lower bulk density.

The majority of the pore sizes range from 0.005-0.01 μm, with all the samples (except OK Springer U) having greater than 35% pore diameter in that range. Interestingly, the greater the sample depth, the higher the quantity of smaller pores is present. To show this, OK Springer 2L has 44.8% of its pores in the 0.003-0.005 micro-meter range, while samples OK Springer 2M and 2U have 28.4% and 12.5% respectively in that range. This trend is seen throughout every pore range (Figures 4-7 and 4-8). The

MICP apparatus is limited to 60,000 psi and can only detect pore sizes down to 3 nm. Figure 4-5 and 4-6 below show intrusion is still occurring at maximum pressure (60,000 psi), indicating that there are pores smaller than 3 nm in the majority of the samples still being invaded at maximum pressure. Pores smaller than 3 nm probably do not have a drastic influence on production due to the miniscule amount of fluids that can move through them. Figures 4-3 and 4-2 show pore throat size vs incremental pore area. These graphs demonstrate that as the pores get smaller, the more mercury is able to invade the sample, therefore taking up more area. There is very little mercury invading into the sample in the beginning. As the pressure increases, so does the mercury intrusion, causing the mercury to invade smaller and smaller pores which make up the majority of the pores within the sample. On the far left showing the smallest pore throats, the incremental pore area spikes at around 0.01 μm pore diameter, showing that the majority of the pores in the sample are smaller than 0.01μm and can contain larger amounts of mercury than the other pore sizes combined.

The tortuosity values are used to determine geometrical aspect of fluid movement inside porous media. They are defined as the ratio of actual distance traveled between two points to the minimum distance between the two points (Gommes et al., 2009). High tortuosity values indicate that fluids will have a difficult time getting through the sample, while lower values indicate that fluids can pass more easily through the formation. There is a range of tortuosity values shown in Table 4-3 between 3.53 in OK Springer L and 6.59 in OK Springer 2M. Using the same procedures, the Barnett shale has a tortuosity range of 1.99 to 12.2 with the majority being 8-12 (Hu et al, 2015b), indicating that it takes significantly less effort for fluids to move through the Goddard compared to the Barnett Shale. As shown in Table 4-3, tortuosity increases with depth of

sample in each well, indicating that the stratigraphically shallower samples are able to migrate fluids easier than the deeper samples.

There has been a significant amount of work determining pore networks and sizes in shales. Organic matter pores smaller than 10 nm in size are difficult to see on SEM images, while MICP cannot differentiate between different pore types (Lohr et al, 2015). Organic matter pores are generally sub-μm in size and are proven to be a significant component of shales such as the Barnett, Woodford, and Horn River (Lohr et al, 2015).While it is difficult to distinguish pore types using MICP measurements alone, adding imbibition data can increase the accuracy. This thesis attempts to make a general determination of pore types. Maxwell Pommer and Kitty Milliken described the differences in pore sizes in the Eagle Ford Shale. They concluded that organic matter based pores have an average size of 13.2 nm or smaller and mineral based pores have an average size of 30.2 nm (Pommer and Milliken, 2015). Using this data, the percentage of pores 13.2 nm or smaller in the in the Goddard shale is shown in Figures 4-9 and 4-10. This coincides with the idea of mineral pores being destroyed during early compaction by cementation and infill, thus transitioning the majority of pores from mineral grain pores to organic matter pores (Pommer and Milliken, 2015). While this method lacks complete accuracy, it can still be seen that the majority of pores in the Goddard are organic matter hosted compared to mineral hosted due to their sub-μm size.

Table 4-3 MICP Results

Sample ID	Sample Depth (MD')	Dimensions (cm)	Sample Mass (g)	Total pore area ($\frac{m^2}{g}$)	Median pore-throat diameter (Area) (µm)	Bulk density ($\frac{g}{cm^3}$)	Apparent (skeletal) density ($\frac{g}{cm^3}$)	Effective Porosity (%)	Pores smaller than 3nm?	Permeability (mD)	Tortuosity
OK Springer U	12,809'	Fragments	2.2689	1.80	0.0124	2.47	2.63	6.07	No	16.7	6.35
OK Springer M	12,847'	~1 cm cube	2.3635	14.9	0.0065	2.30	2.47	6.91	Yes	0.797	6.59
OK Springer L	12,871'	~1 cm cube	2.2215	14.8	0.0053	2.42	2.58	6.00	Yes	0.207	3.53
OK Springer 2U	12,945'	~1 cm cube	3.1504	8.07	0.0066	2.67	2.81	5.27	Yes	0.437	5.19
OK Springer 2M	13,010'	~1 cm cube	3.1664	16.7	0.0053	2.28	2.43	6.23	No	0.259	5.75
OK Springer 2L	13,046'	~1 cm cube	2.5220	7.29	0.0042	2.41	2.47	2.48	Yes	0.896	6.03

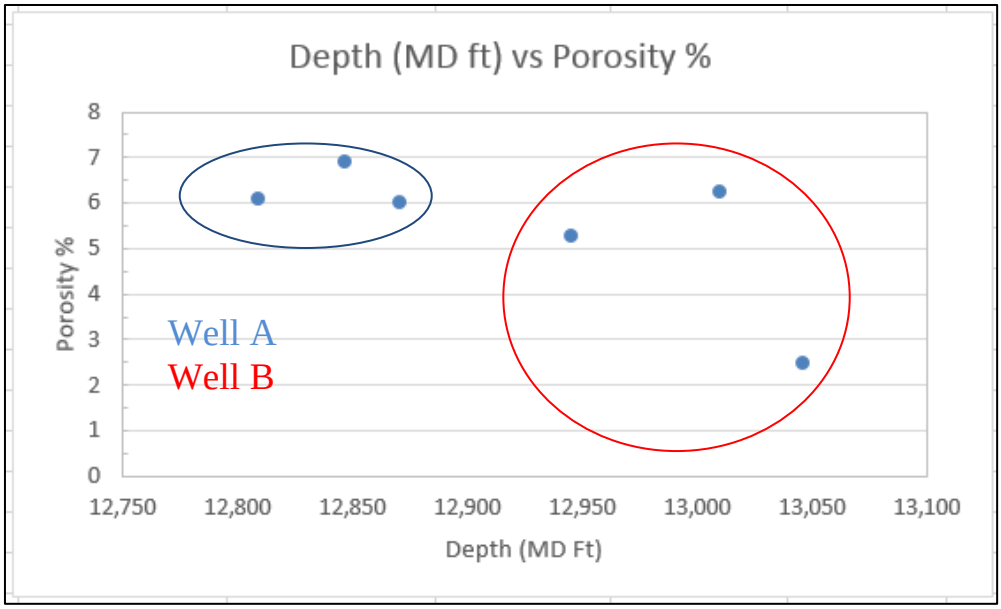

Figure 4-1 Goddard shale Depth (MD Ft) vs Porosity %.

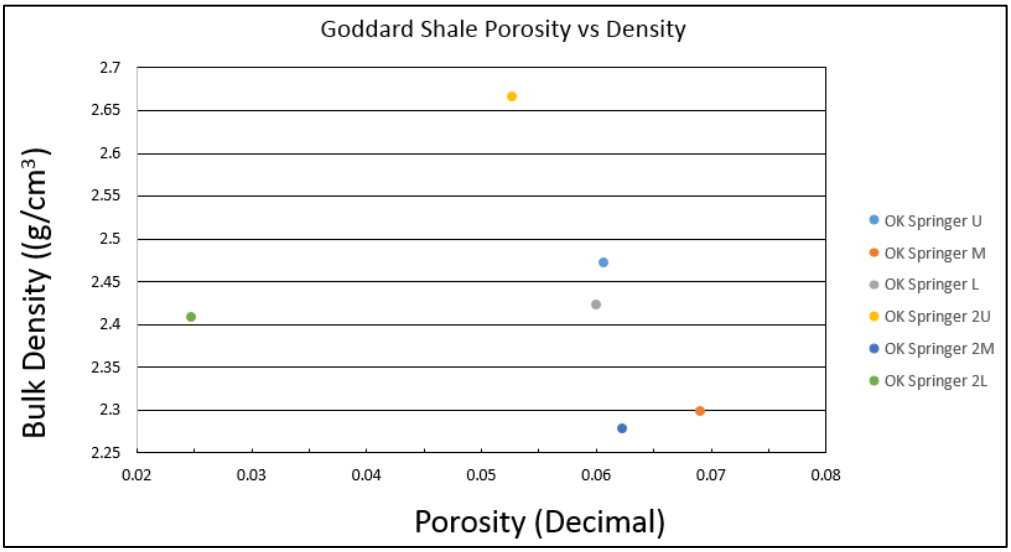

Figure 4-2 Density vs Porosity in the Goddard shale.

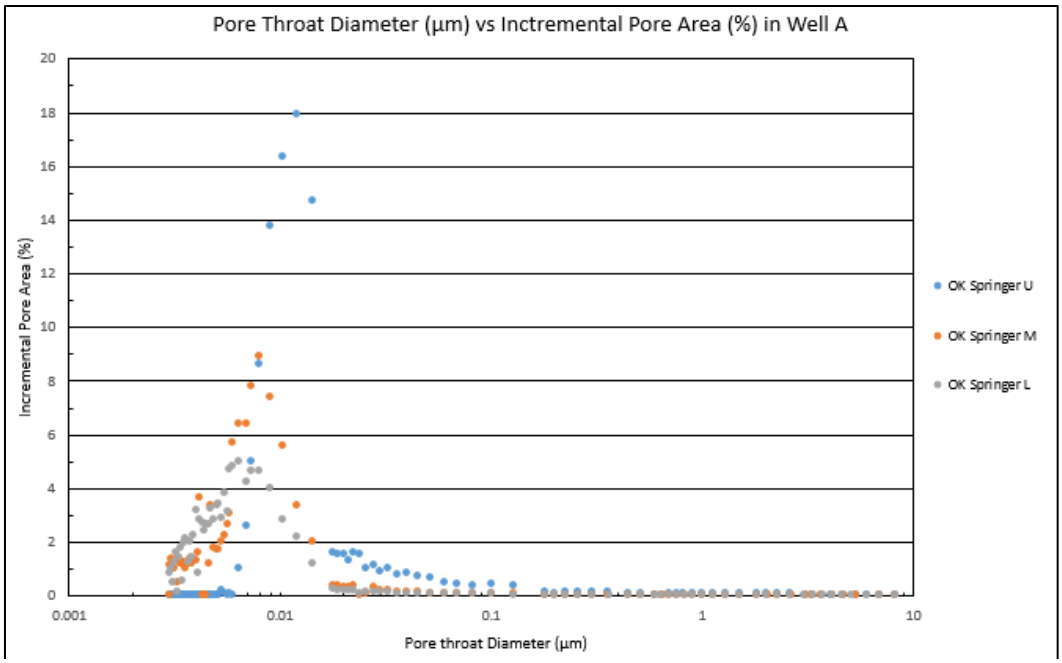

Figure 4-3 Pore Throat Diameter (µm) vs Incremental Pore Area in Well A.

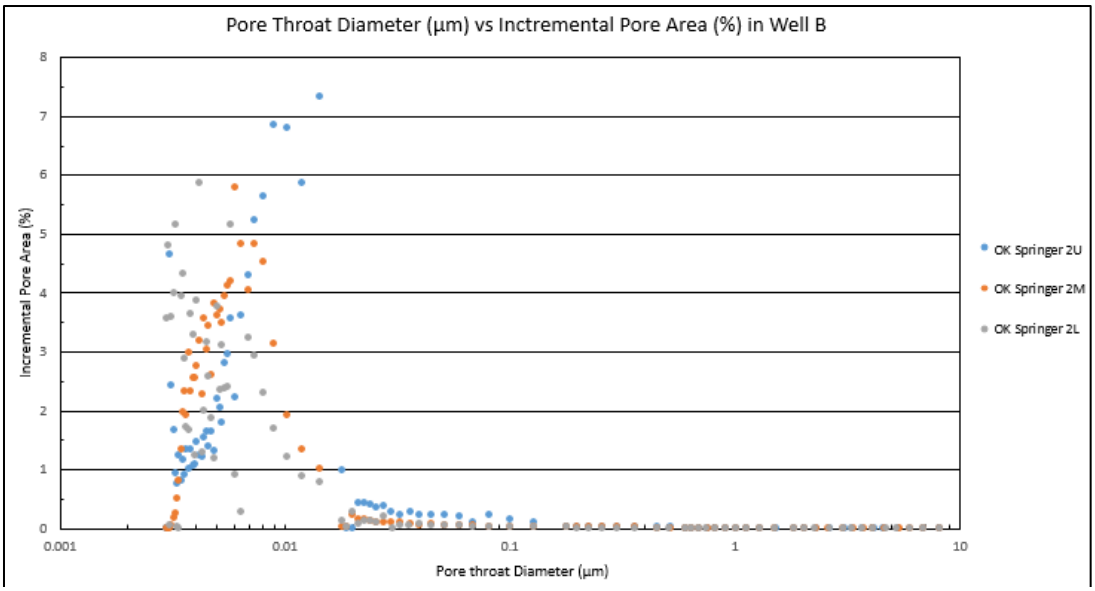

Figure 4-4 Pore Throat Diameter (µm) vs Incremental Pore Area in Well B.

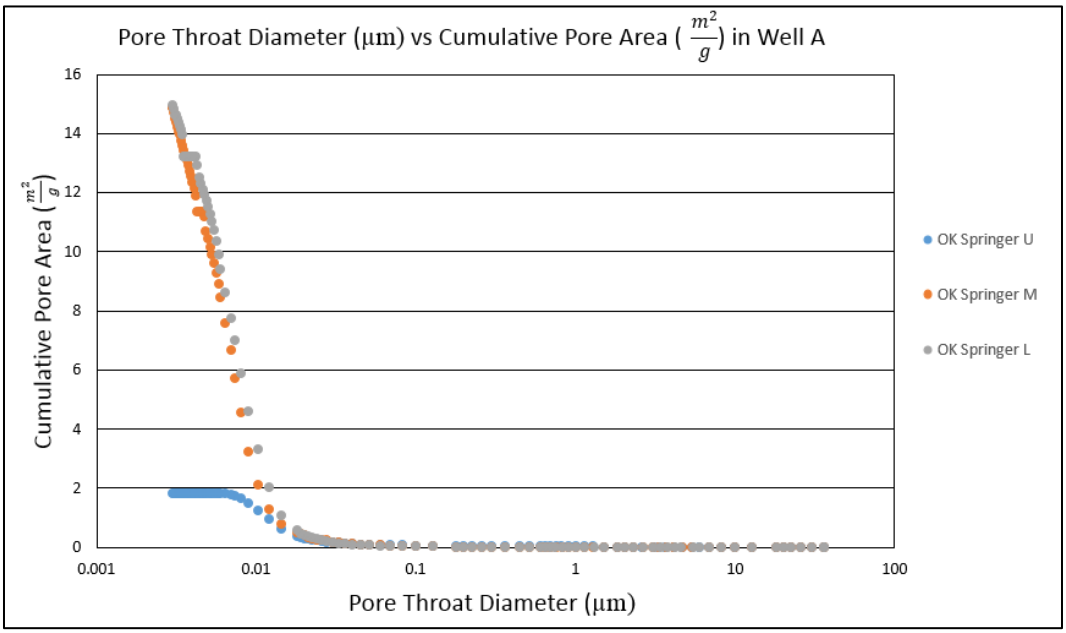

Figure 4-5 Pore Throat Diameter (µm) vs Cumulative Pore Area (m^2/g) in Well A.

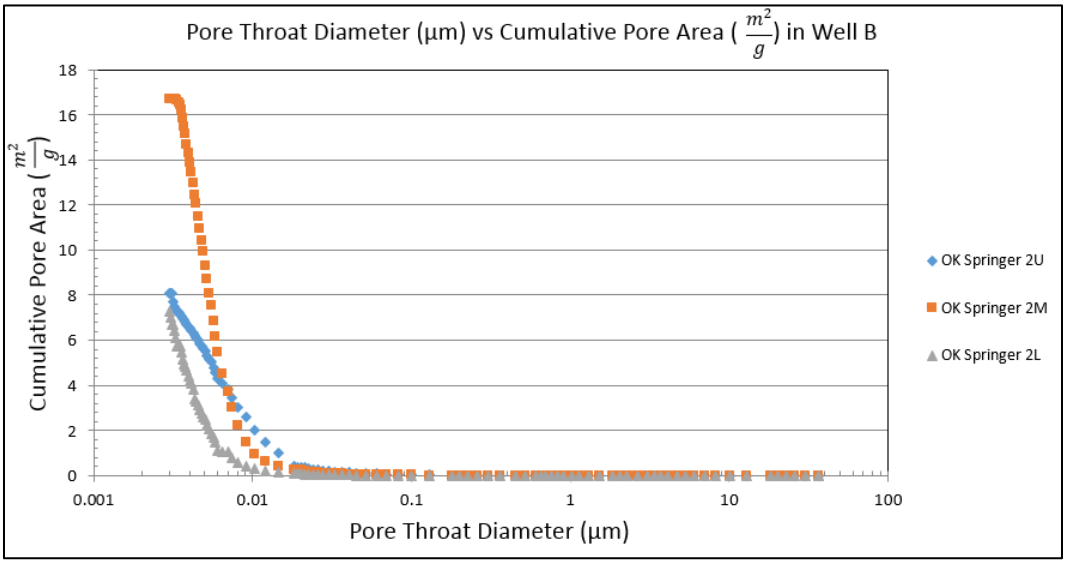

Figure 4-6 Pore Throat Diameter (µm) vs Cumulative Pore Area (m^2/g) in Well B.

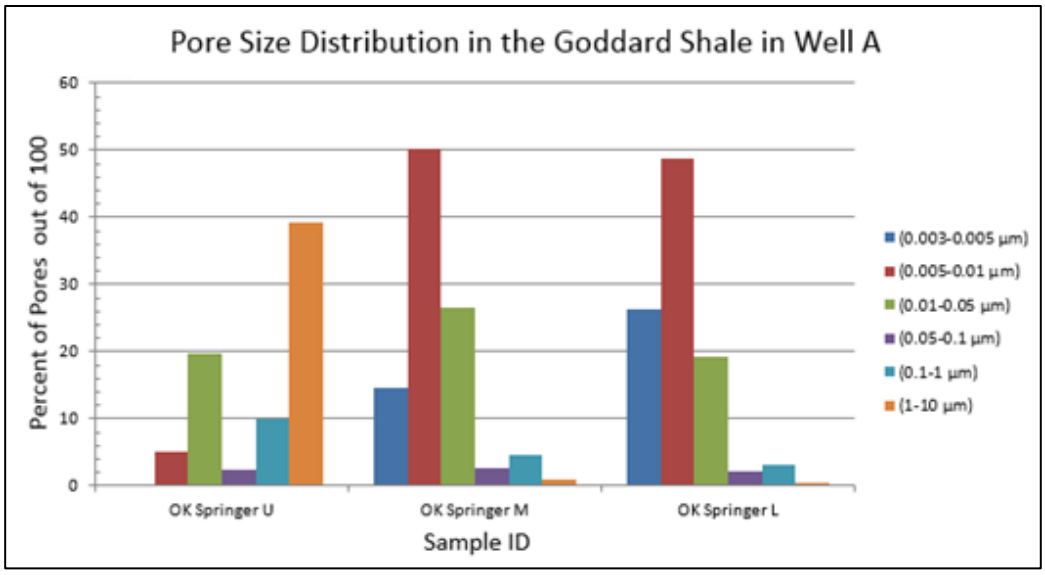

Figure 4-7 Pore Throat Diameter Distribution in the Goddard shale in Well A.

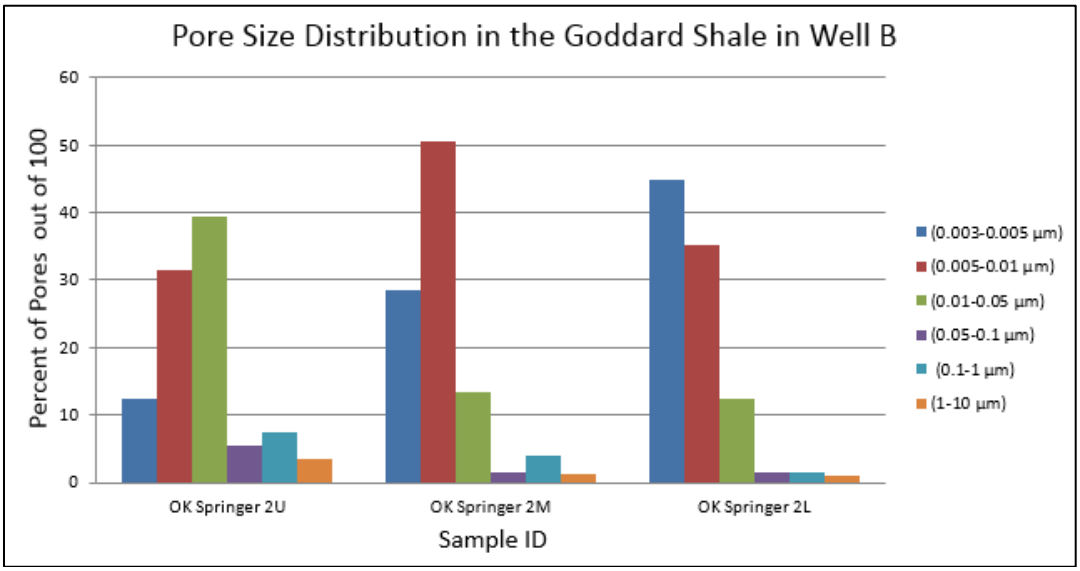

Figure 4-8 Pore Throat Diameter Distribution in the Goddard shale in Well B.

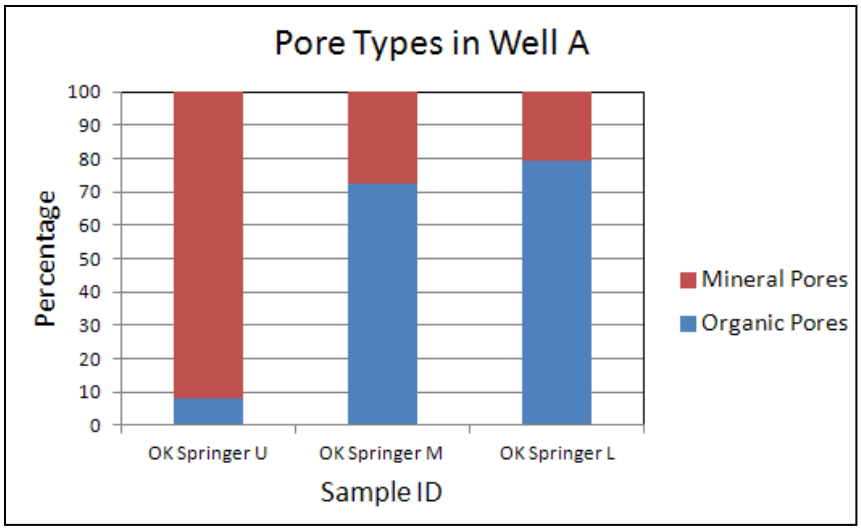

Figure 4-9 Organic vs Mineral Pores in the Goddard shale in Well A. Organic pores are assumed to be 13.2 nm and smaller.

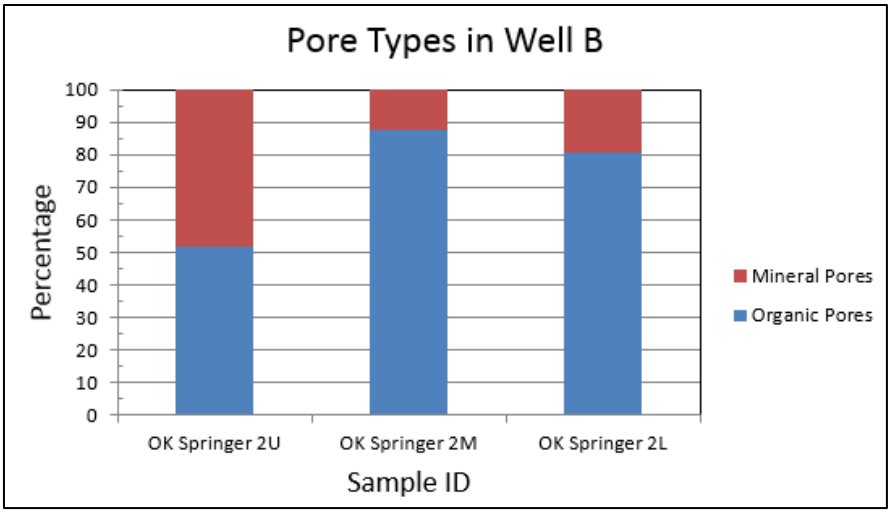

Figure 4-10 Organic vs Mineral Pores in the Goddard shale in Well B. Organic pores are assumed to be 13.2 nm and smaller.

4-3 Spontaneous Fluid Imbibition and Vapor Adsorption

Spontaneous imbibition is the process of a fluid imbibing into the face of a sample over a period of time. The fluids used in this study were: DI water, n-decane (organic iodide), and API brine to study the Goddard shales' fluid affinities and repulsions. The epoxy on 4 of the 6 sides of the sample allowed fluids to move from one face to its opposite without escaping through the sides. DI water tests were triplicate measurements consisting of a 12, 24, and 48 hour time periods with a drying period in between to remove any residual water in connected pore spaces. Their final slopes were averaged and shown in Table 4-4. There could be three slope values as shown in Figures 4-11, 4-12 and 4-13; the first slope is the initial uptake of fluid onto the surface, followed by an intermediate slope and final slope. There is scatter in data at the beginning of the tests caused by the sample settling into the fluid. The intermediate slope is associated with the fluid migrating up the exterior of the sample along with the edge porosity. The final slope provides the most accurate information and demonstrates the samples ability to move fluid through the pores. The slope values are a representation of the pore connectivity and efficiency of fluid to move through the pores over a given time period and have no units associated with them since they are logarithms.

Tracers containing n-decane and API brine tests were single tests over a 24 hour time period prior to freeze-drying in liquid nitrogen and storage for later use. The n-decane fluid consisted of a mixture of tracers consisting of n-decane with organic-iodide and organic-rhenium to be used in future research using Laser Ablation Inductively Coupled Mass Spectrometry (LA-ICP-MS). The API brine fluid was composed of 8% NaCl and 2% $CaCl_2$ with tracers composed of cesium – iodide, samarium - iodide, antimony and ruthenium-complexes. The tracers used in both API brine and n-decane are easily recognized by the LA-ICP-MS machine to be used in the future.

The DI water average final imbibition slopes ranged from 0.145 in OK Springer 2L to 0.265 in OK Springer 2M. These values show that the Goddard has low pore connectivity when in contact with water and API brine, consistent with the wettability tests. API brine had slopes of 0.478, 0.502, 0.339, 0.170, and 0.174 which are smaller overall than that of n-decane which had slopes of 0.461, 0.499, 0.530, 0.752, and 0.545 with an average of 0.557. The n-decane test for OK Springer 2M

(Figure 4-12) shows a final slope of 0.170, this slope is representative of the n-decane reaching the sample top and supported by visual observation at the conclusion of the testing period. For this reason, the slope of 0.752 is deemed the final slope for OK Springer 2M. The drastic difference between the water and n-decane slope values that indicate the Goddard has stronger and more effective pore connectivity for oil based fluids such as n-decane.

Table 4-4 Spontaneous Imbibition Test Results

Sample ID	Depth (MD ft')	Testing Fluid	Sample Dimensions (cm)	Final Imbibition Slope (s)
OK Springer M	12,847'	DI Water	1.029 L × 0.958 W × 1.079 H	0.157; 0.252
		API Brine	1.039 L × 0.911 W × 1.043 H	0.478
		N-Decane	1.021 L× 1.040 W × 1.008 H	0.461
OK Springer L	12,871'	DI Water	1.032 L × 1.047 W × 1.052 H	0.145; 0.185; 0.349;
		API Brine	1.033 L × 0.925 W × 1.065 H	0.502
		N-Decane	1.029 L × 1.078 W × 0.994 H	0.499
OK Springer 2U	12,945'	DI Water	1.110 L × 1.040 W × 0.960 H	0.129; 0.204
		API Brine	1.040 L × 1.040 W × 1.030 H	0.339
		N-Decane	1.010 L × 1.090 W × 1.100 H	0.530
OK Springer 2M	13,010'	DI Water	1.000 L × 1.010 W × 0.970 H	0.200; 0.275; 0.321
		API Brine	0.970 L × 1.210 W × 1.070 H	0.170
		N-Decane	0.990 L × 0.930 W × 1.080 H	0.752
OK Springer 2L	13,046'	DI Water	1.040 L × 1.020 W × 1.095 H	0.096; 0.194
		API Brine	0.990 L × 1.050 W × 0.950 H	0.174
		N-Decane	0.990 L × 1.030 W × 1.050 H	0.545

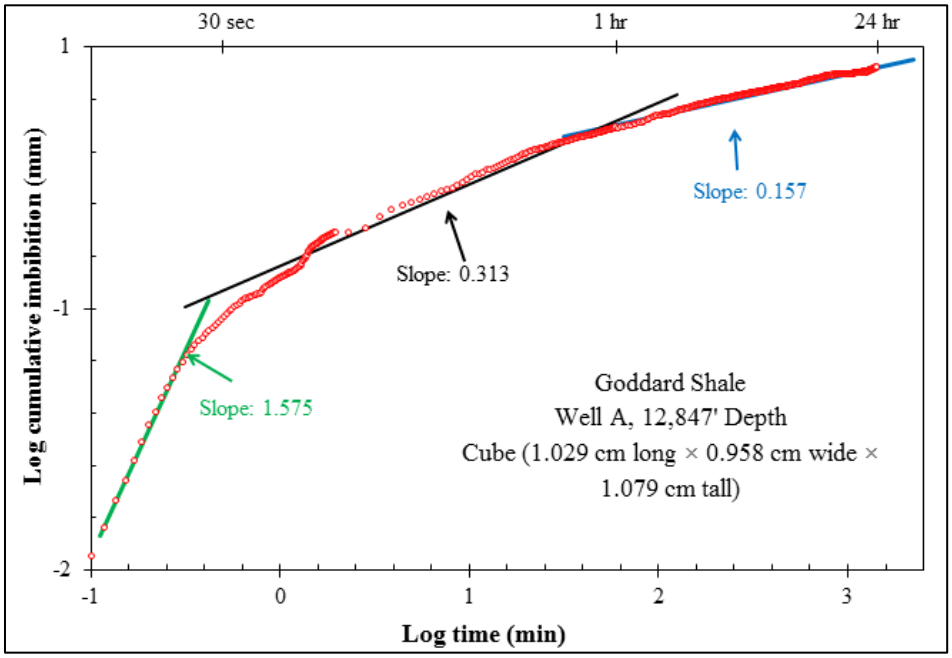

(A) Well A, M (12,847')

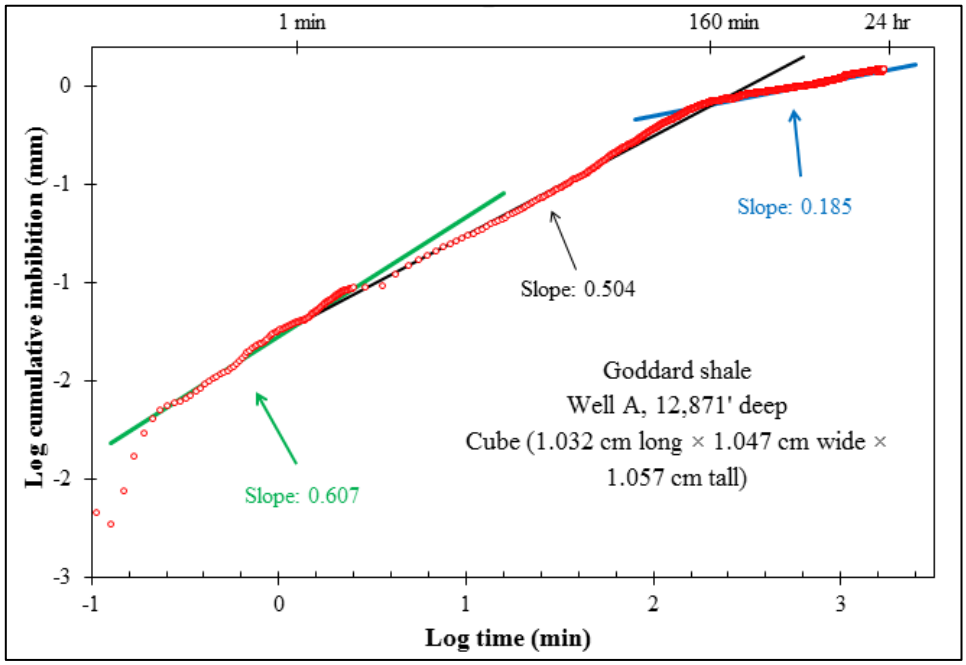

(B) Well A, L (12,871')

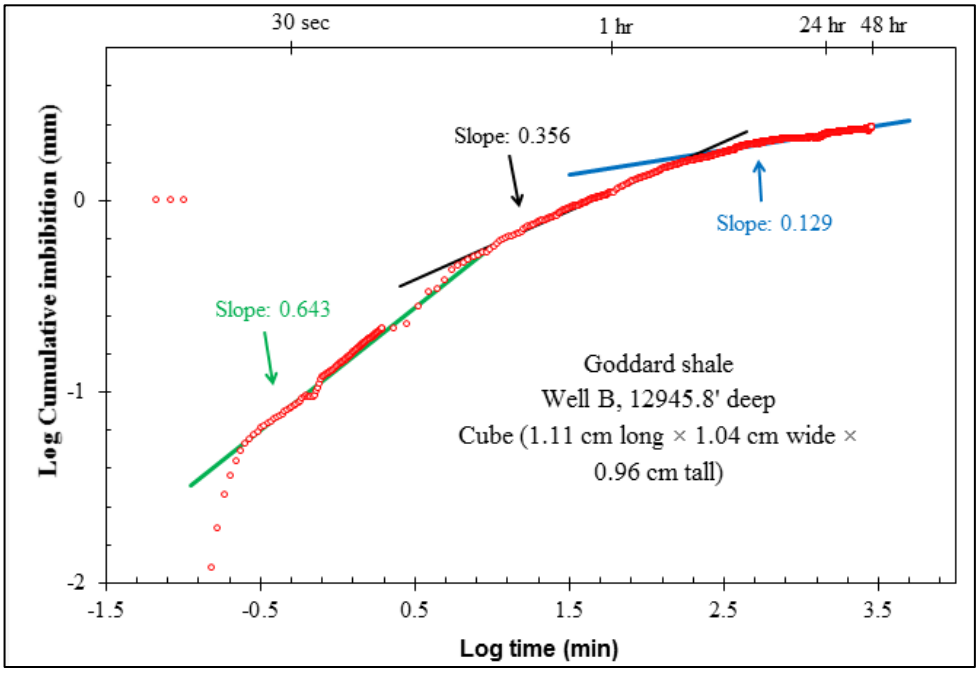

(C) Well B, 2U (12,945')

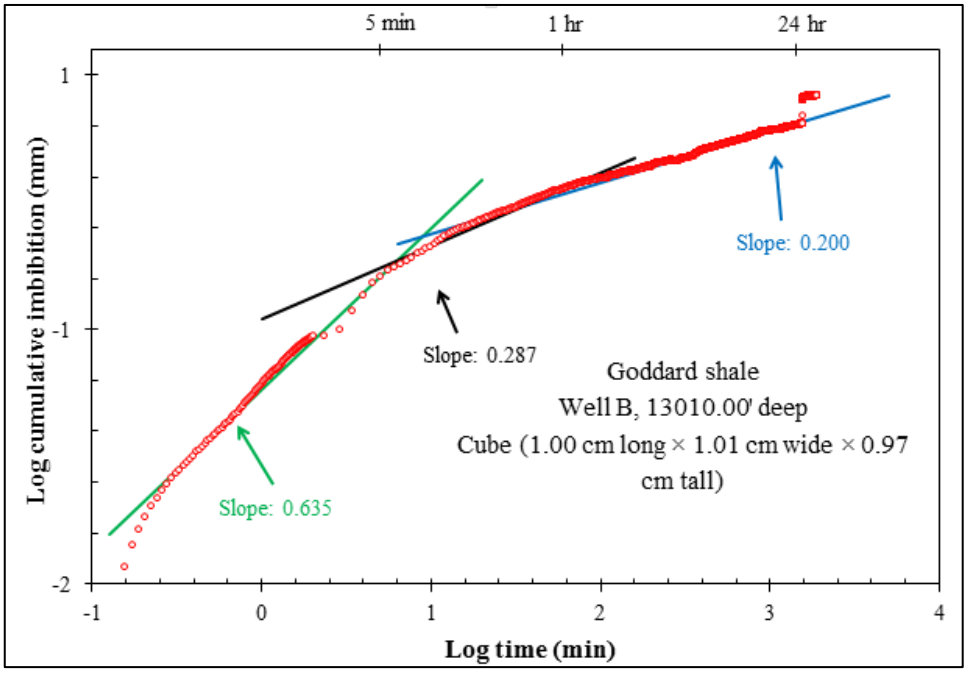

(D) Well B, 2M (13,010')

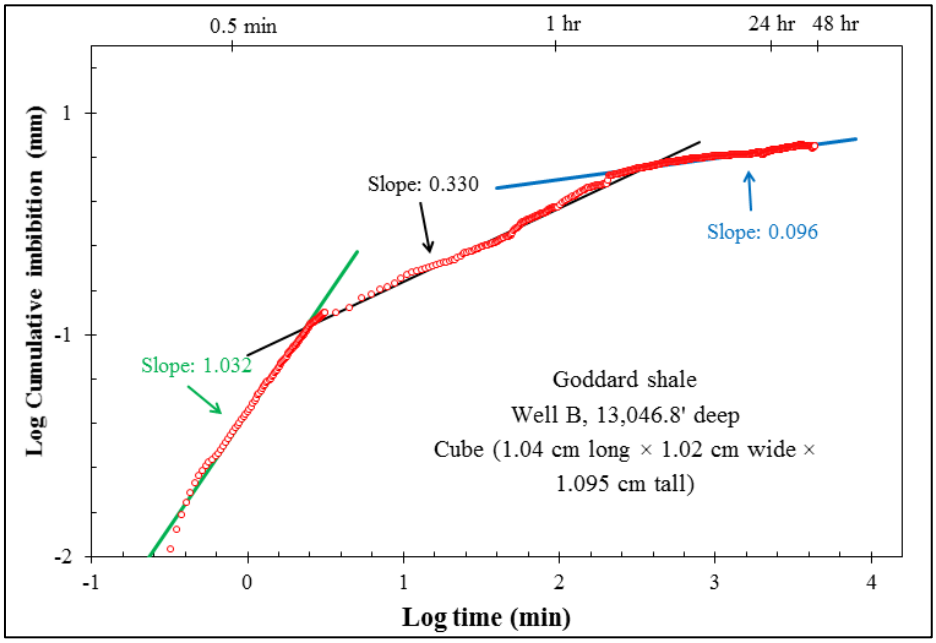

(E) Well B, 2L (13,046')

Figure 4-11 DI Water Imbibition Results. (A) OK Springer M; (B) OK Springer L; (C) OK Springer 2U; (D) OK Springer 2M; (E) OK Springer 2L.

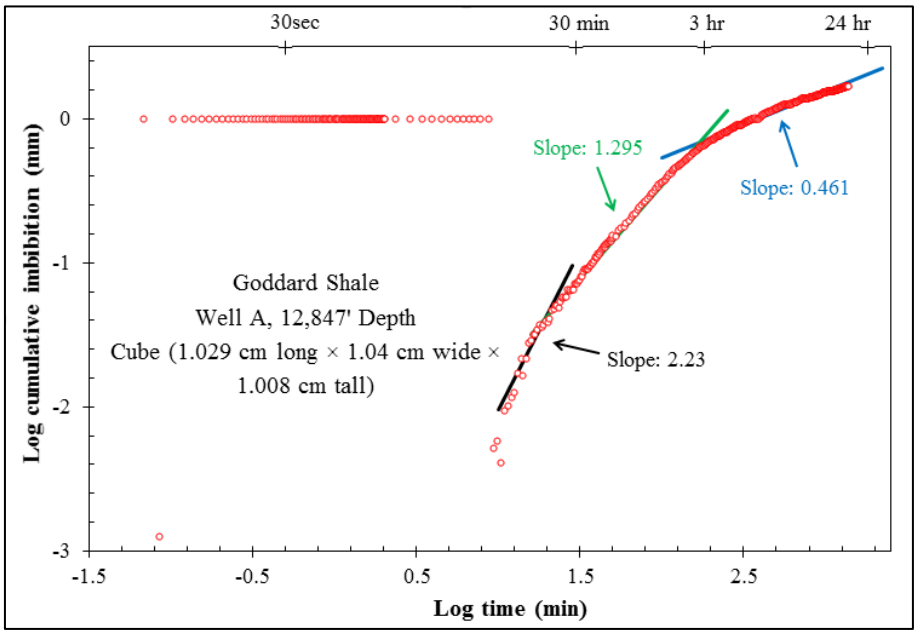

(A) Well A, M (12,847')

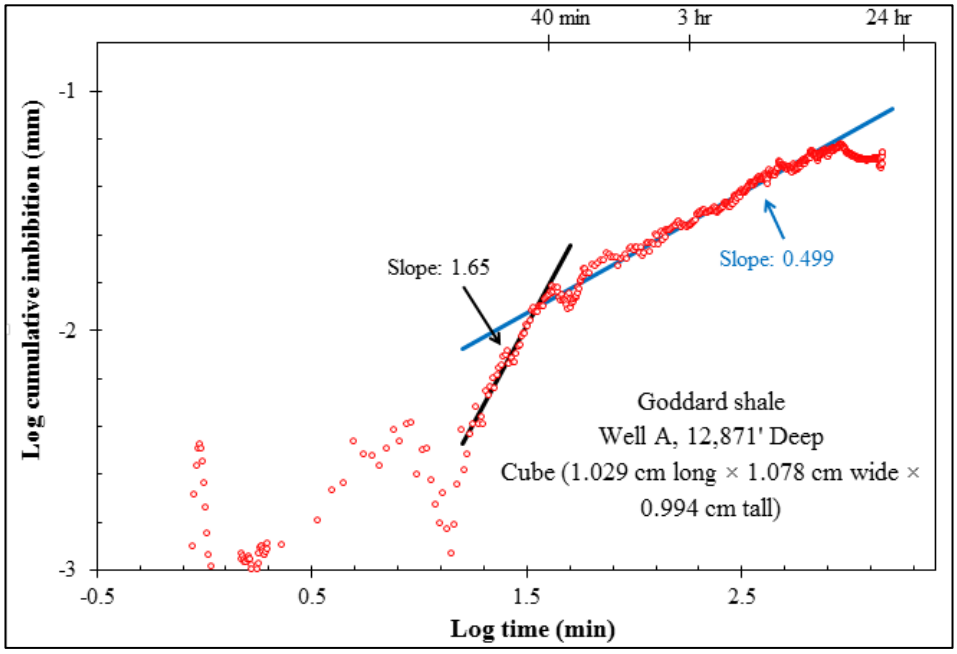

(B) Well A, L (12,871')

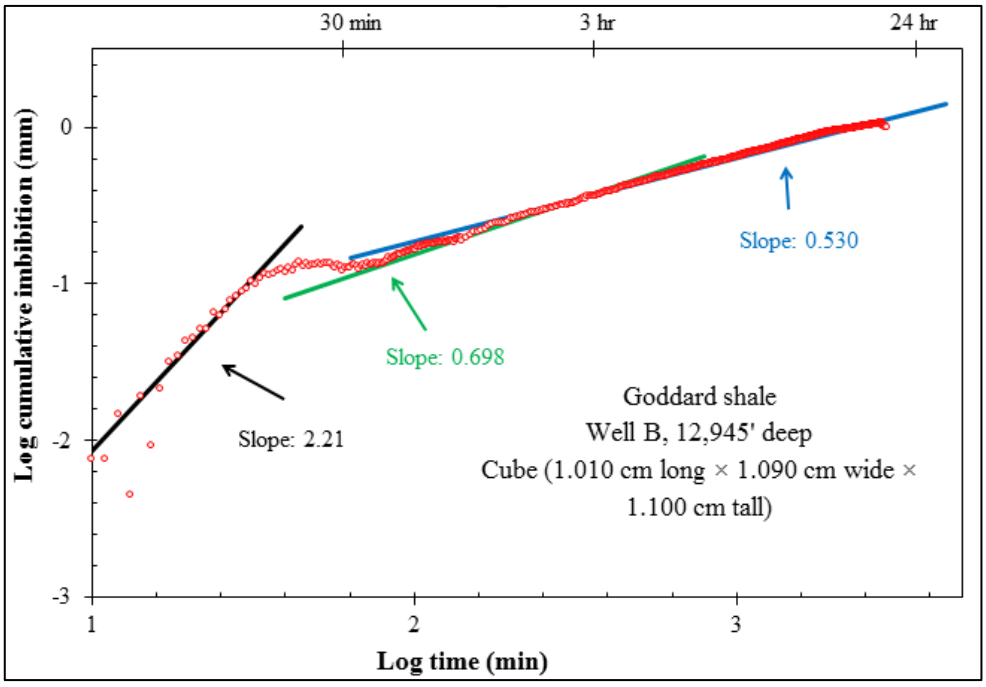

(C) Well B, 2U (12,945')

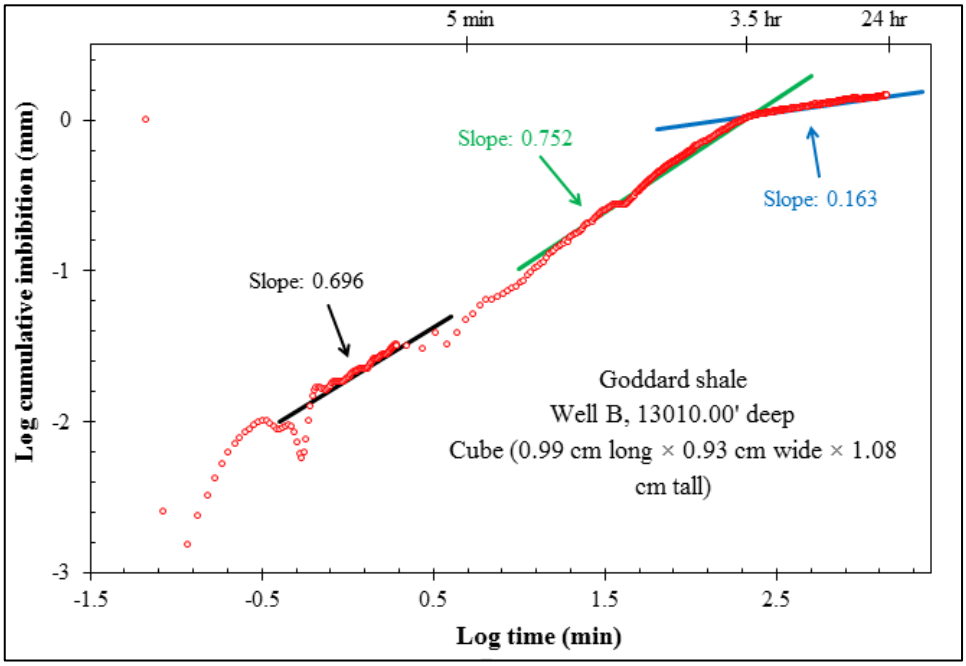

(D) Well B, 2M (13,010')

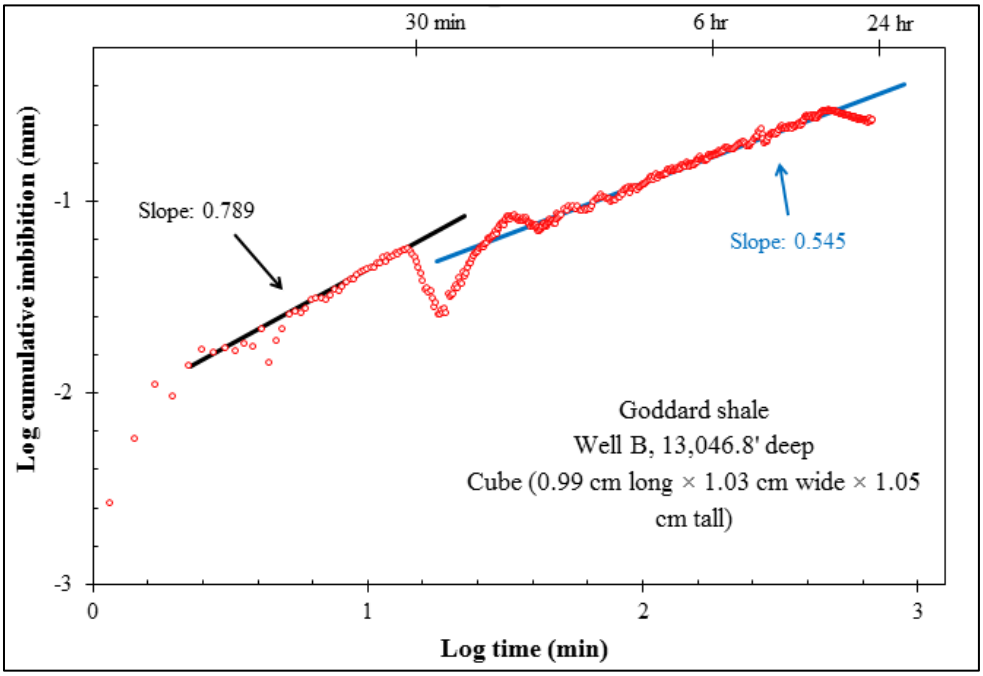

(E) Well B, 2L (13,046')

Figure 4-12 N-Decane Spontaneous Imbibition. (A) OK Springer M; (B) OK Springer L; (C) OK Springer 2U; (D) OK Springer 2M; (E) OK Springer 2L.

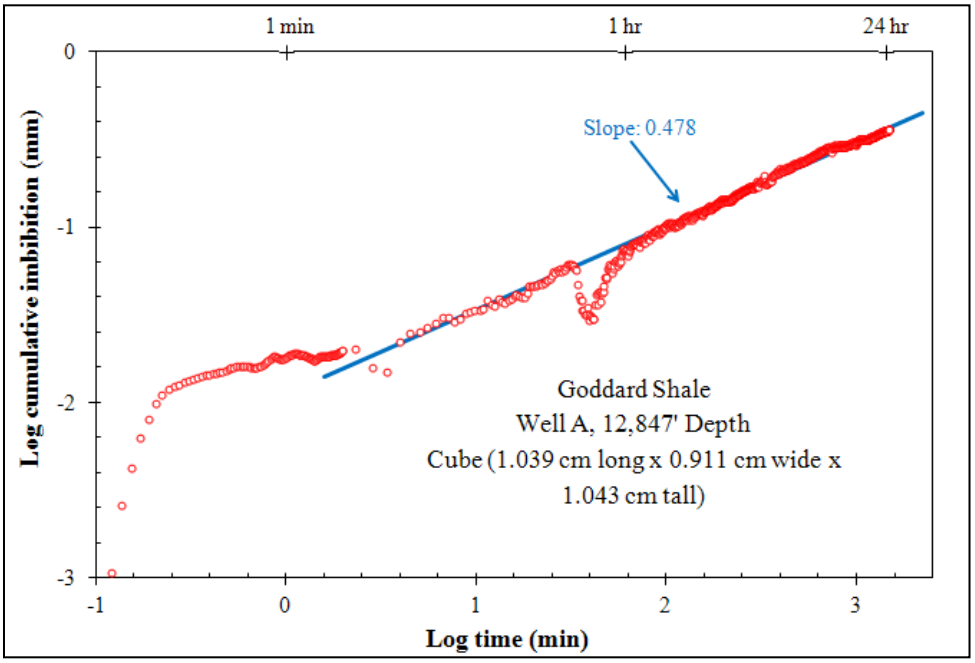

(A) Well A, M (12,847')

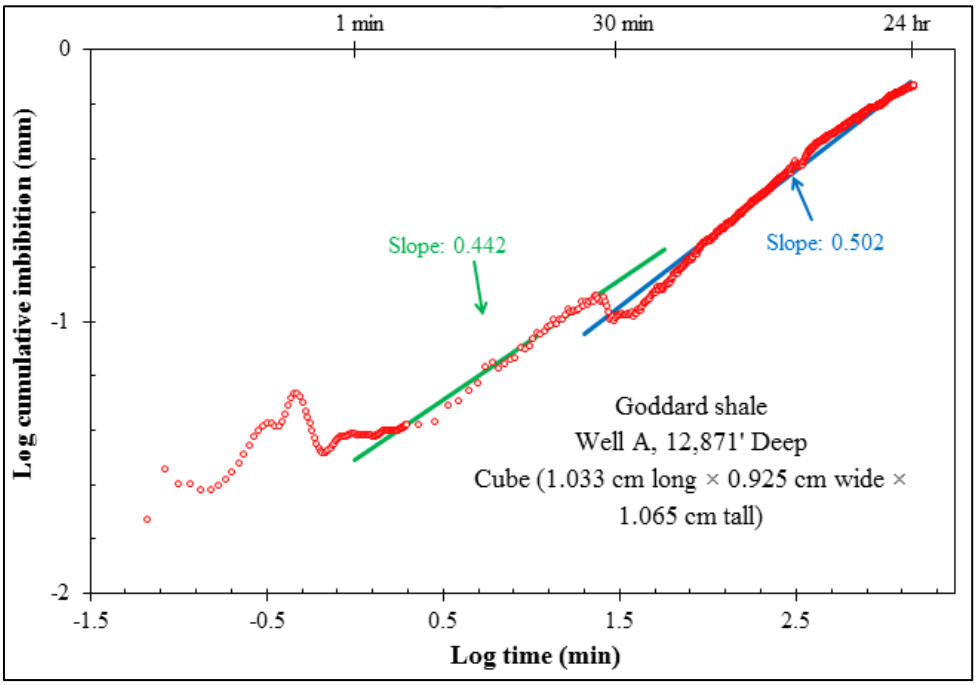

(B) Well A, L (12,871')

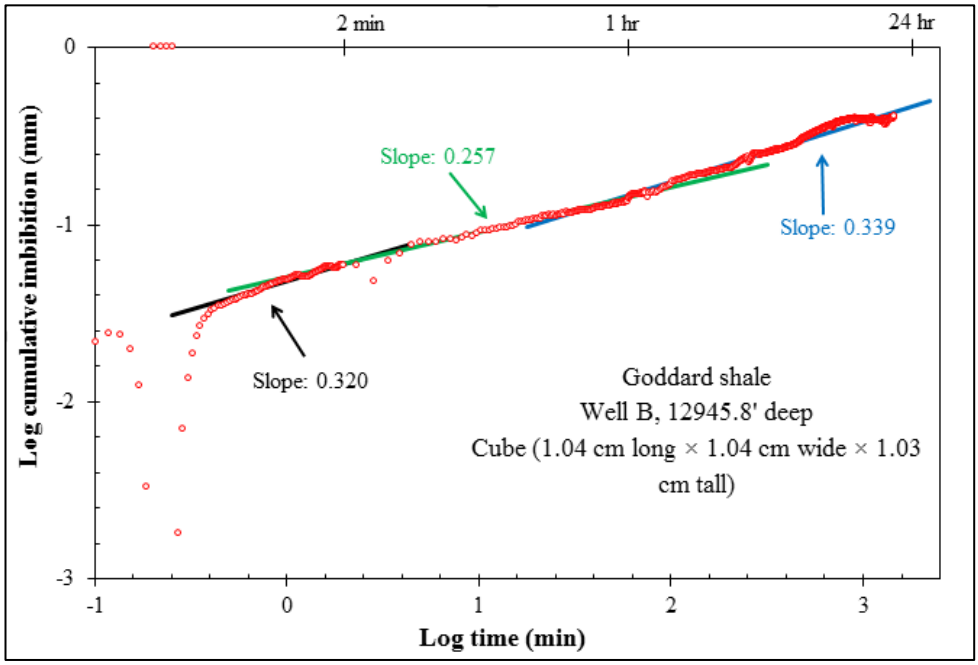

(C) Well B, 2U (12,945')

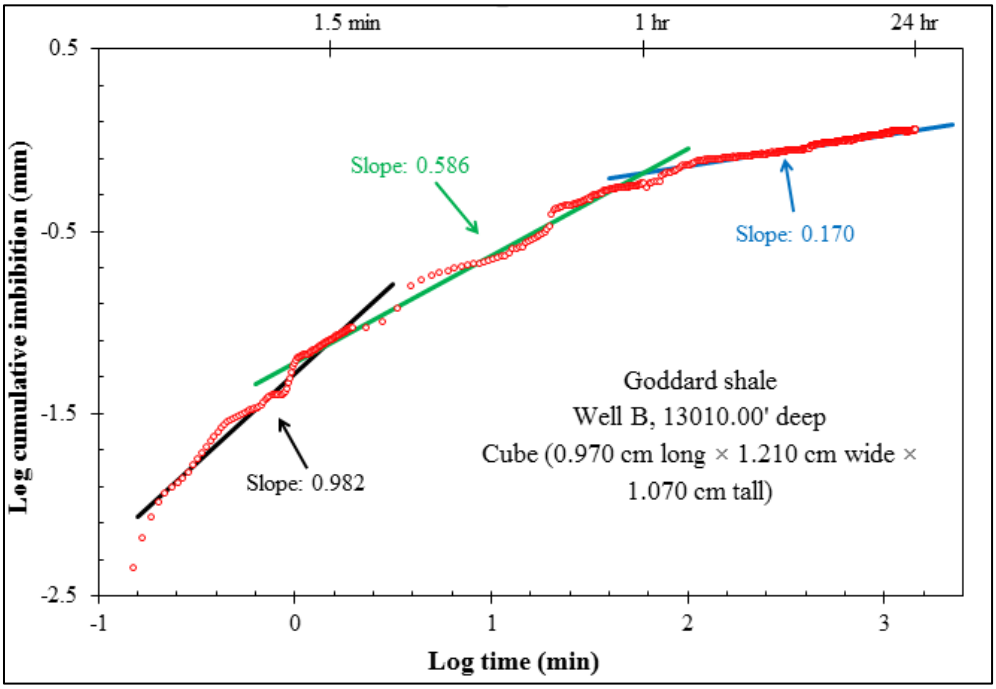

(D) Well B, 2M (13,010')

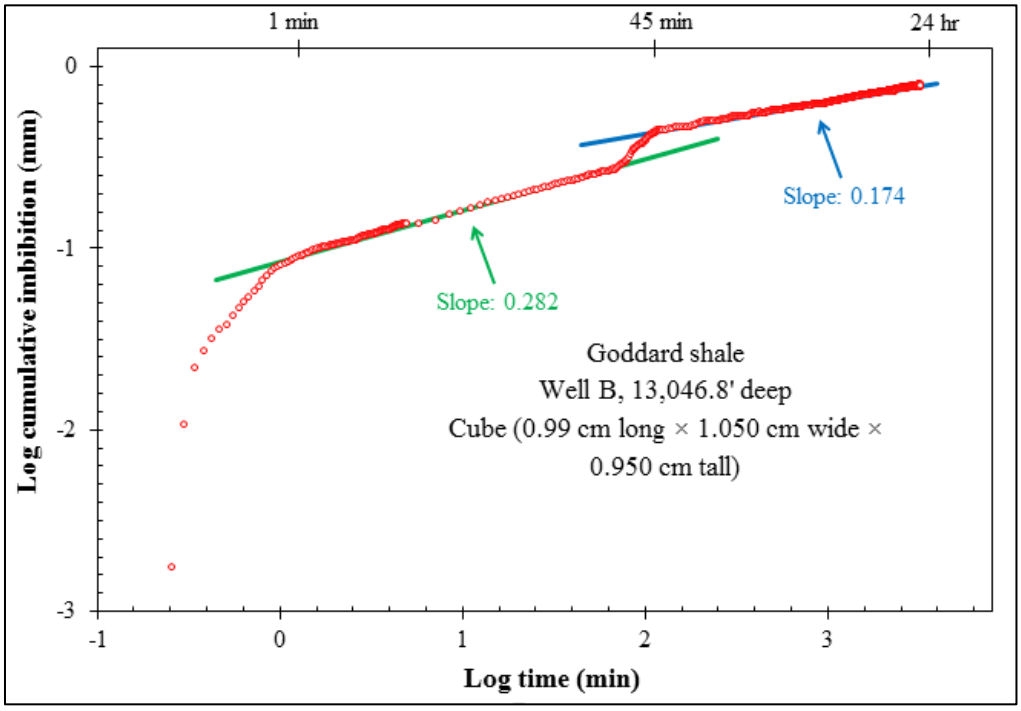

(E) Well B, 2L (13,046')

Figure 4-13 API Brine Spontaneous Imbibition. (A) OK Springer M; (B) OK Springer L; (C) OK Springer 2U; (D) OK Springer 2M; (E) OK Springer 2L.

DI Water Vapor Adsorption

Vapor adsorption in the Goddard shale shows an increasing trend with depth (Figure 4-14). While none of the samples achieved complete adsorption, a relationship between depth of sample and effectiveness of adsorption is observed. The deeper the sample, the higher both the intermediate and final slopes (Table 4-5). The slope values do not have units and merely approximate efficiency of vapor migration and pore connectivity. Lower values represent less vapor adsorbing in the sample while higher values reflect a quicker rate of adsorption and better pore connectivity. The results indicate that there could be a link between the depth within the formation and water quantity (Figure 4-14). The shallower samples had an overall lower water vapor adsorption rate than the deeper ones, seen by their lower final slope values in Table 4-5. The scatter at the beginning of the tests seen on the graphs below can be associated with a slight

shaking of the sample hanging from a wire as the apparatus reaches equilibrium. Figures 4-15 below are the vapor adsorption results graphs after 7 days of hanging inside the chamber.

Table 4-5 DI Water Vapor Adsorption

Sample ID	Depth (MD ft')	Sample Dimensions (cm)	Intermediate Slope	Intermediate Slope Duration	Final Slope	Final Slope Duration	Final Fluid Saturation (%)
OK Springer M	12,847'	1.029 L × 0.958 W × 1.079 H	0.781	1 min – 10 hrs	0.407	10 -150 hrs	332
OK Springer L	12,871'	1.032 L × 1.047 W × 1.052 H	0.992	45 min - 2 hrs	0.488	2 – 158 hrs	336
OK Springer 2U	12,945'	1.110 L × 1.040 W × 0.960 H	0.761	45 min – 6 hrs	0.487	6 – 154 hrs	548
OK Springer 2M	13,010'	1.000 L × 1.010 W × 0.970 H	0.956	45 min – 2 hrs	0.495	2 – 158 hrs	325
OK Springer 2L	13,046'	1.040 L × 1.020 W × 1.095 H	1.084	1 hr – 2 hrs	0.499	2 – 158 hrs	351

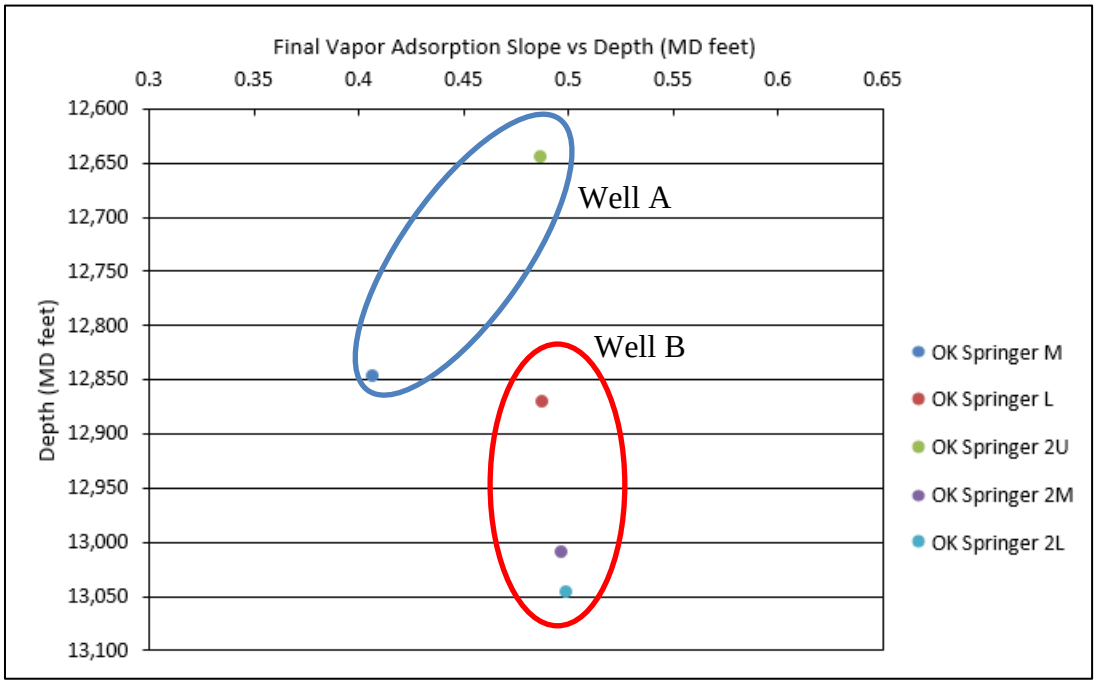

Figure 4-14 Vapor Adsorption Final Slope vs Depth (MD feet).

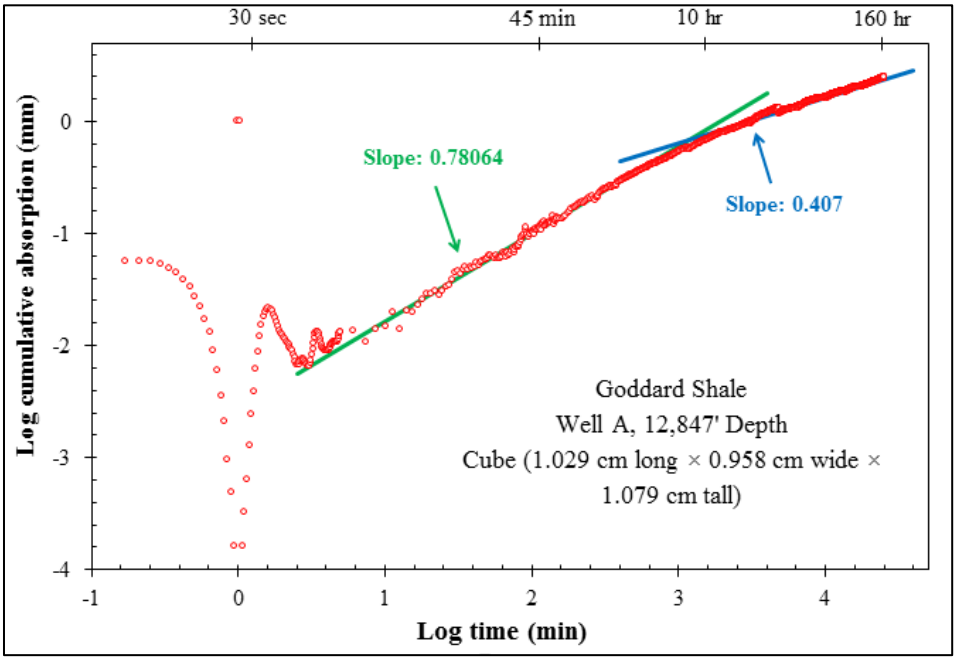

(A) Well A, M (12,847')

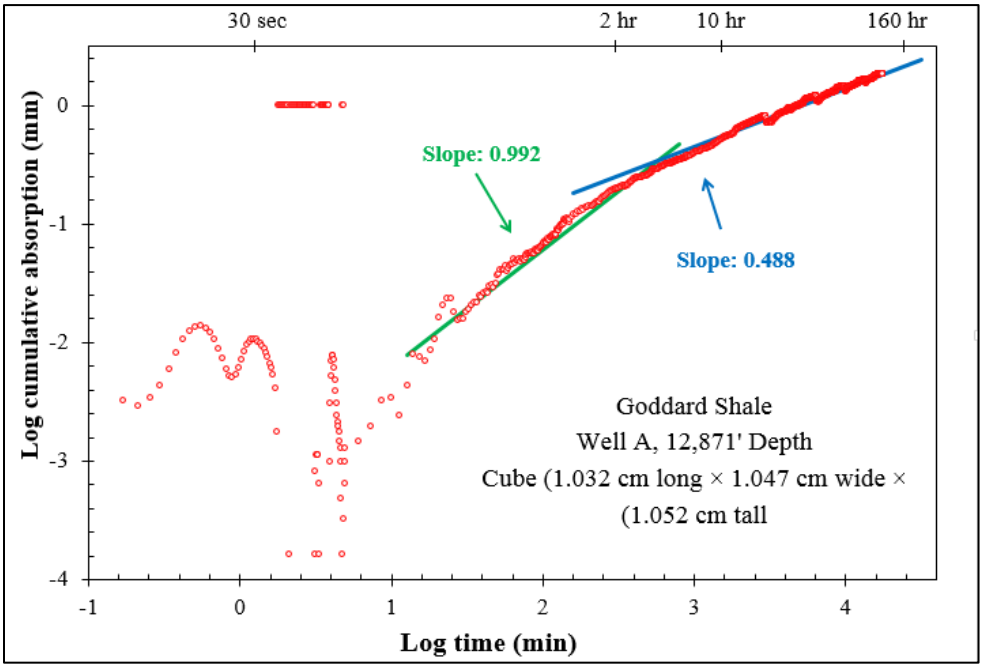

(B) Well A, L (12,871')

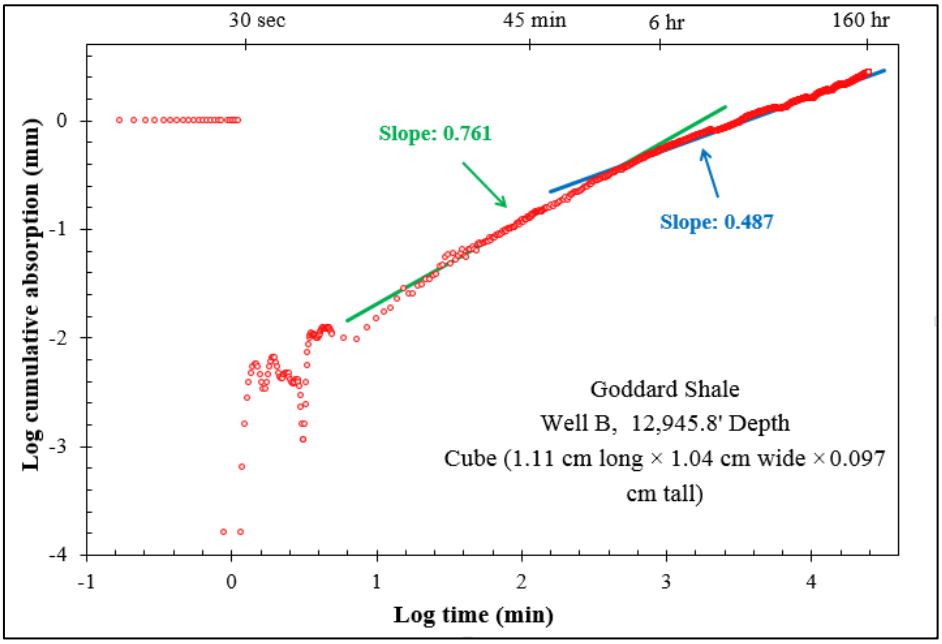

(C) Well B, 2U (12,945')

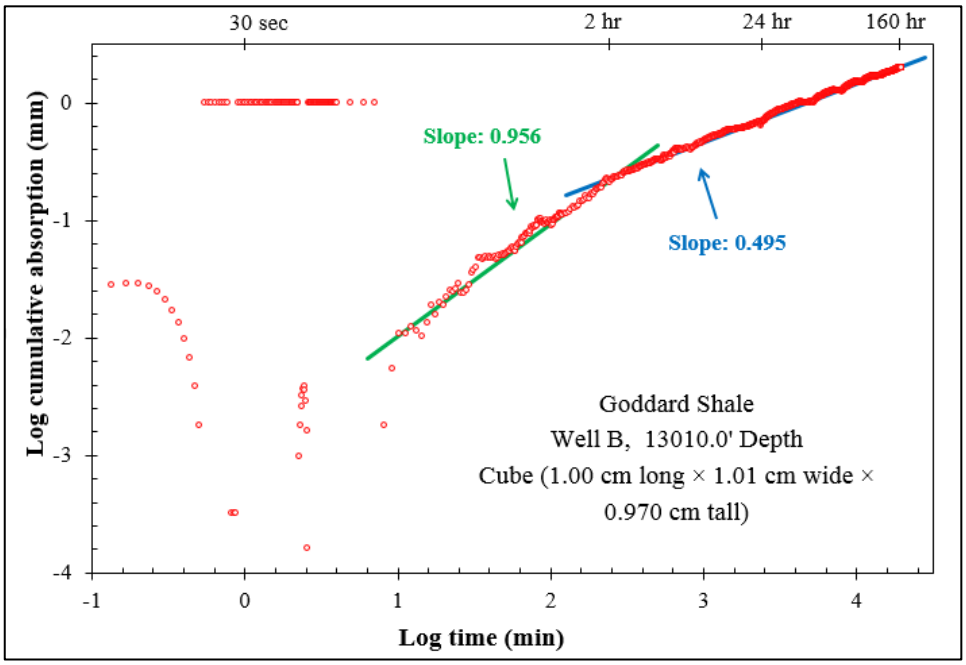

(D) Well B, 2M (13,010')

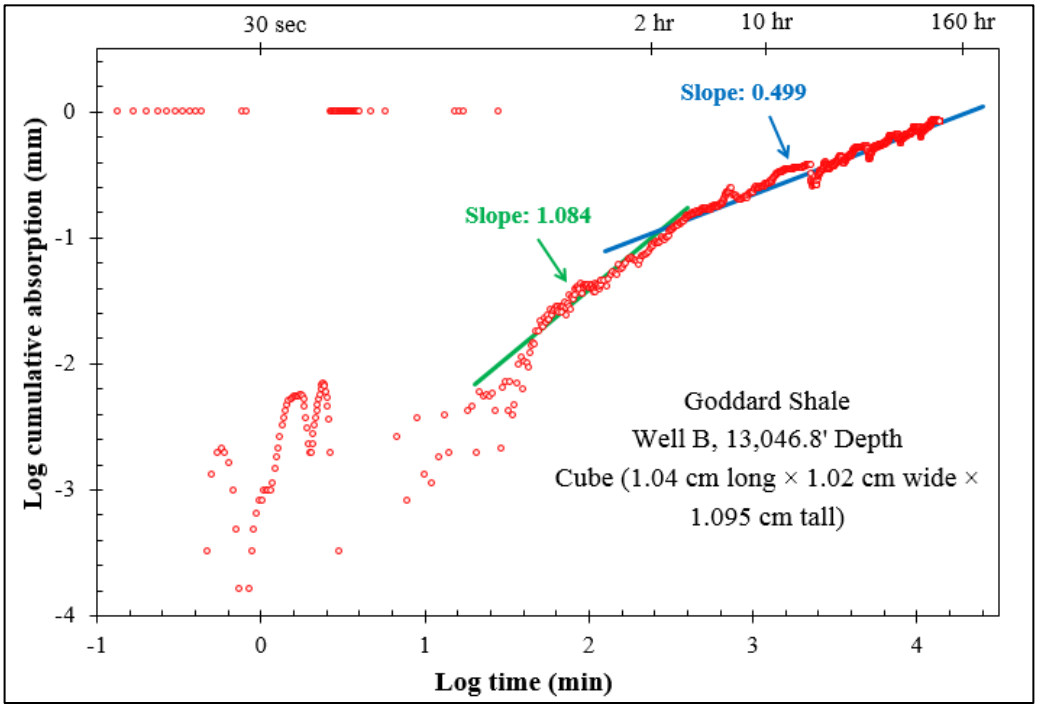

(E) Well B, 2L (13,046')

Figure 4-15 DI Water Vapor Adsorption. (A) OK Springer M; (B) OK Springer L; (C) OK Springer 2U; (D) OK Springer 2M; (E) OK Springer 2L.

4-4 Discussion and Conclusion

The Goddard shale is still in the exploration stages with more challenges ahead. Unconventional shales are well-known for rapid decline rates, but as knowledge of these formations increase, so will their production rates and overall success. This study examined the Goddard shales' fluid absorption and migration to better determine pore connectivity and geometry which may be useful in predicting the decline rates and recovery factors in shale reservoirs.

Core samples from two wells located in the South Central Oklahoma Province (SCOOP) were used to determine fluid absorption and migration in the Goddard shale. The experimental methods used: wettability, mercury injection capillary pressure (MICP), and spontaneous imbibition. With a porosity average of 5.49%, a permeability average (excluding OK Springer U) of 0.519 mD, and the majority of pore throat diameters ranging from 0.005 – 0.01 μm, the Goddard shale contains primarily organic pores. Imbibition methods simulate reservoir conditions and show that the formation has a strong affinity for oil, indicating that the Goddard would be a strong candidate for a shale reservoir rock. Average n-decane final imbibition slopes were 0.557, higher than the average DI water slope of 0.214 and API brine slope of 0.333, which reinforces the Goddard's ability to act as a reservoir rock by preferring oil to water.

4-5 Recommendations

There is still much to be learned regarding pore connectivity and fluid migration (from tracers-containing brine and n-decane, and follow-up detection of tracers by LA-ICP-MS) in the Goddard shale. More samples need to be analyzed using different techniques such as FIB-SEM, CT scanning and mineralogy techniques to better understand this producing formation and how hydrocarbons migrate through the shale matrix. Measurement of TOC and mineralogy would also be beneficial to further understanding the Goddard shale. In addition, gas sorption isotherm tests are needed to quantify smaller pore sizes (<100 nm) to complement the MICP results.

References

Ball, M., Henry, M., Frezon, S. 1991. Petroleum geology of the Anadarko Basin Region, Province (115), Kansas, Oklahoma, and Texas. United States Geological Survey, 19(76): 88-450.

Bennison, A. 1956. Springer and related rocks of Oklahoma. Tulsa Geological Society Digest, 24: 111-115.

Blakey, R. 2014. North America Paleogeography Maps. http://cpgeosystems.com/index.html.

Boyd, D. 2008. Stratigraphic guide to Oklahoma oil and gas reservoirs. Oklahoma Geological Society.

Brewer, J., Good, R., Oliver, J., Brown, L., Kaufman, S. 1983. COCORP profiling across the Southern Oklahoma Aulacogen: Overthrusting of the Wichita Mountains and compression within the Anadarko Basin. Geological Society of America, 11(2): 109-114.

Buckley, S., and M. Leverett. 1942. Mechanism of fluid displacements in sands. Society of Petroleum Engineers, 146(1): 107–116.

Chaudhuri, B., Jessen, K., Tsotsis, T. 2010. Water inversion in shale: A preliminary study. USC Viterbi Research Symposium.

Chrisman, J. 2009. Depositional setting, facies, and petroleum geology of Boatwright Sandstones (Springer Group) in parts of Caddo, Canadian, and Blaine Counties, OK. M.S. Thesis, Department of Science, Oklahoma State University, USA.

Chukwuma, F. 2015. Nanopetrophysics of the Utica Shale, Appalachian Basin, Ohio, USA. M.S. Thesis, Department of Science, University of Texas at Arlington, USA.

Continental Resources Investor Presentations. 2014. http://investors.clr.com/phoenix.zhtml?c=197380&p=irol-presentations.

DrillingInfo, 2015.

Elias, M. 1951. Upper Mississippian and Lower Pennsylvanian Formations of South-Central Oklahoma. Petroleum Geology of Southern Oklahoma, 1(16): 56-134.

Gao, Z., Hu, Q., Peng, S., Ewing, R. 2012. Pore structure inhibits gas diffusion in the Barnett Shale. AAPG Search and Discovery Article #50609.

Gommes, C., Bons, A., Blacher, S., Dunsmuir, J. 2009. Practical methods for measuring the tortuosity of porous materials from binary or gray-tone tomographic reconstructions. AlChE Journal, 55(8): 2000-2012.

Hager, J. 1998. Steam drying of porous media. Ph.D. Thesis, Department of Chemical Engineering, Lund University, Sweden.

Handy, L. 1960. Determination of effective capillary pressures for porous media from imbibition data. Petrol. Trans. AIME, 219: 75–80.

Henry, M., and T. Hester. 1995. Anadarko Basin Province (058). National Assessment of Unites States Oil and Gas Resources, 51p.

Hu, Q., and R. Ewing. 2014. Integrated experimental and modeling approaches to studying the fracture-matrix interaction in gas recovery from Barnett Shale. Final Report, Research Partnership to Secure Energy for America (RPSEA), National Energy Technology Laboratory, Department of Energy, 91p.

Hu, Q., Ewing, R., Rowe, H. 2015a. Low nanopore connectivity limits gas production in the Barnett Formation. Journal of Geophysical Research: Solid Earth. Doi: 10.1002/2015JB012103.

Hu, Q., Hu, W., Gao, Z., Liu, S., Liu, X., Zhou, W. 2015b. Pore structure and tracer migration behavior of typical American and Chinese shales. Petroleum Science, 12(4): 651-663.

Hugman, R., and F. Vidas. 1987. Oil and Gas resources of the Mid-Continent Region: Energy and Environmental Analysis. Incorporated, Arlington, VA, 140p.

Johnson, K. 1998. Anadarko Basin Symposium. Oklahoma Geological Society 90, 289p.

Katz, A., and A. Thompson. 1986. A quantitative prediction of permeability in porous rock. Physical Review B, 34: 8179–8181.

Katz, A., and A. Thompson. 1987. Prediction of Rock Electrical Conductivity from Mercury Injection Measurements. Journal of Geophysical Research: Solid Earth, 92(B1): 599-607.

Kaufmann, J. 2010. Pore space analysis of cement-based materials by combined nitrogen sorption - Wood's metal impregnation and multi-cycle mercury intrusion. Cement Concrete Comp. 32(7): 514-522.

Laudon, R. 1958. Chesterian and Morrowan rocks in the McAlester Basin of Oklahoma. Oklahoma Geological Survey 46.

Lee, Y., and D. Deming. 2002. Overpressures in the Anadarko Basin, Southwestern Oklahoma: Static or Dynamic. The American Associated of Petroleum Geology 86(1): 145-160.

Lohr, S., Baruch, E., Hall, P., Kennedy, M. 2015. Is organic pore development in gas shales influenced by the primary porosity and structure of thermally immature organic matter? Department of Earth and Planetary Sciences, Macquarie University, North Ryde, Australia. Elsevier Ltd. Organic Chemistry, 87: 119-132.

Lopez, R., and A. Soria. 2007. Kinematical description of the spontaneous imbibition processes. IASME/WSEAS international conference, Athens, Greece.

Ma, S., Morrow, N., Zhang, X. 1999. Characterization of wettability from spontaneous imbibition measurements. Petroleum Society of Canada, 38(13): 1–8.

Mattox, C., and J. Kyte. 1962. Imbibition oil recovery from fractured water drive reservoir. Soc. Petrol. Eng. J., 2(2): 177–184.

Menchaca, M. 2014. Oklahoma Oil and Gas: wWodford SCOOP wells have stamina. Drilling Info.

Micrometrics. 2011. Autopore IV 9500 Operators Manual.

Mitchell, J. 2012. The Anadarko Basin: Oil and Gas Exploration - Past, Present, and Future. Oklahoma Geological Survey. Oklahoma Structural and Stratigraphic Oil and Gas Workshop PowerPoint.

Nash, S. 2014. The Springer Shale: A sleeping giant? Search and Discovery, 10664.

Northcutt, R., and J. Campbell. 1995. Geologic provinces of Oklahoma. Oklahoma Geological Survey.

OGS Editors. 2014. Continental testing Springer Shale potential. Oil and Gas Journal, Online.

Oklahoma Corporate Commission Imaging Database. 2015. http://imaging.occeweb.com/

Peace, H. 1965. The Springer Group of the Southeastern Anadarko Basin in Oklahoma: Shale Shaker, 15(5): 81-99.

Philip, J. 1957. The theory of infiltration: 4. Sorptivity and algebraic infiltration equations. Soil Science 84(3): 257–265.

Pommer, M., and K. Milliken. 2015. Pore types and pore size distribution across thermal maturity, Eagle Ford Formation, Southern Texas. American Association of Petroleum Geologists, 99(9): 1713-1744.

Rice, A. 1993. Depositional environment, petrology, and compartmentalization of Cunningham and Britt Sandstones in parts of Caddo, Grady, and Comanche Counties, Anadarko Basin, Oklahoma. Unpublished M.S. Thesis, Oklahoma State University, 192p.

Smith, P., Walter, H., Craig, W. 1995. Regional correlations and reservoir characterization studies of the Springer Group in the Anadarko Basin Area of Western Oklahoma. AAPG Mid-Continent Section Meeting.

Straka, J. 1972. Conodont evidence of age of Goddard and Springer Formations, Ardmore Basin, Oklahoma. The American Association of Petroleum Geologist Bulletin 55(6): 1087-1099.

Swanson, B. 1981. A simple correlation between permeabilities and mercury capillary pressures. Society of Petroleum Engineers, 33(12) 2498-2504.

Tomlinson, C., and W. McBee. 1962. Pennsylvanian sediments and orogenies of Ardmore District, Oklahoma. Petroleum Geology of Southern Oklahoma, 2(19): 3-52.

Washburn, E. 1921. Note on a method of determining the distribution of pore sizes in a porous materials. Proceedings of the National Academy of Sciences 7: 115-116.

Westheimer, J. 1954. The Goddard Formation, in petroleum geology of southern Oklahoma, A symposium sponsored by the Ardmore Geological Society. American Association of Petroleum Geologist, Tulsa, 1: 292-396.

Wilson, L. 1996. Palynological evidence for Mississippian age of the Springer Formation. Ardmore Geological Society, Guidebook Pennsylvanian of the Ardmore Basin, 20-24p.

Xie, X., and N. Morrow. 2001. Oil recovery by spontaneous imbibition from weakly water-wet wocks. Petrophysics, 42(4): 313-322.

Zhou, J., Ye, G., Breugel, K. 2010. Characterization of pore structure in cement–based materials using pressurization-depressurization cycling mercury intrusion porosimetry (PDC-MIP). Cement and Concrete Research, 40 (7): 1120-1128.

Biographical Information

Paul Huggins was born on August 10, 1992 in Grapevine, Texas. He graduated from Grapevine High School in 2010 and went on to study geology at the University of Arkansas, Fayetteville. Upon graduation in May 2014, he returned to Grapevine, Texas and started his masters' degree in August 2014 at the University of Arlington in earth and environmental sciences. He worked at Expro Minerals as a geotechnical consultant in Fort Worth, TX from August 2014 to October 2015. He then began work as geological consultant for GeoPetra Partners LLC in October 2015 and graduated in December 2015 with his masters in earth and environmental sciences.